Predictions for the Circumgalactic Medium of Low-mass, Star-forming Galaxies

THESIS

submitted in partial fulfillment of the
requirements for the degree of

MASTER OF SCIENCE
in
ASTRONOMY

Author :	Brian T. Cook
Student ID :	1780638
Supervisor:	Nastasha Wijers
2nd Supervisor:	Joop Schaye
2nd Corrector :	Marius Cautun

Leiden, The Netherlands, July 29, 2019

Predictions for the Circumgalactic Medium of Low-mass, Star-forming Galaxies

Brian T. Cook

Leiden Observatory, Leiden University
P.O. Box 9500, 2300 RA Leiden, The Netherlands

July 29, 2019

Abstract

Advances in observational techniques have made it possible to analyze the circumgalactic medium (CGM) in previously inaccessible detail. Often defined as the elusive region outside of the disk but within the virial radius of galaxies, the CGM is thought to have a critical role in processes such as galaxy formation and evolution. With the EAGLE cosmological simulations we were able to analyze the CGM of low-mass, star-forming galaxies. We present column density radial profiles for several galaxy classes as well as the associated covering fraction as a function of line-of-sight impact parameter; C IV and Si IV absorbers appear to be more sensitive to varying stellar mass and H I falls off precipitously with decreasing redshift. Additionally, we found profiles for Si IV-weighted local quantities such as temperature and metallicity. Composite flux and optical depth profiles along sightlines passing through low-mass, star-forming EAGLE galaxies at high redshift (both through the galactic nuclei and CGM) were computed with the SpecWizard package for several ions as a function of galaxy frame Hubble velocity such that our mock absorption spectra could readily be compared to observations.

Contents

1 Introduction **1**

1.1 Circumgalactic Medium 1

1.1.1 History and Overview 1

1.1.2 Open Questions 3

1.2 Cosmological Simulations 4

1.2.1 EAGLE 5

1.2.2 Other Software Suites 6

1.3 Low-mass, Star-forming Galaxies 7

1.4 Absorption Spectra 9

1.5 Comparing Simulations to Observations 9

1.6 Brief Overview 10

2 Post-processing Preliminaries **11**

2.1 Pixel Resolution Convergence Tests 14

2.2 Slice Thickness Convergence Tests 16

2.3 Methods of Sampling the Cosmological Box 18

3 Radial Profiles of EAGLE Galaxies **21**

3.1 H I 21

3.2 Si IV and C IV 23

3.3 Density, Temperature, and Metallicity 24

4 The Precursors to Mock Absorption Spectra with EAGLE Data **27**

4.1 Flux and Optical Depth Along a Line-of-sight 28

4.2 Composite Absorption Profiles 31

Version of July 29, 2019– Created July 29, 2019 - 00:59

5 Comparison to Observations 35
5.1 Status of Comparing CGM Simulations to Observations 35
5.2 Circmgalactic Media of EAGLE Galaxies Ready For Direct Comparsion 36

6 Discussion 45
6.1 Unresolved Questions 45
6.2 Future Work 46

7 Conclusion 49

8 Acknowledgements 51

9 Appendix 53
9.1 H I/C IV/Si IV Column Densities and Covering Fractions 53
9.1.1 Metallicity/Density/Temperature 58
9.2 Metal Absorption Spectra 61
9.3 Number of Galaxies in Each Class 65

Version of July 29, 2019– Created July 29, 2019 - 00:59

List of Figures

1.1 A sketch from Tumlinson et al. (2017) of the CGM, its dynamics, and the scales on which these dynamics occur relative to the galactic disk. 2

1.2 A visualization provided in Schaye et al. (2014) of zooming in on a single galaxy found in a much larger structure (100 $\times$ 20 $\times$ 20 Mpc slice). 5

2.1 The virial temperature as a function of total mass and redshift with contours showing the temperatures from the third column of Table 1.1. The relevant temperatures for O VI and Ne VIII exceed the virial temperature of all galaxies considered in this thesis. 13

2.2 Single halo projection of a randomly selected galaxy from the `L0025N0376` box at $z = 0$ with stellar mass $8 < \log(M_\star / M_\odot) < 8.5$. Contours at impact parameters $r = 0.1 R_{\rm vir}, R_{\rm vir}$ are included for reference, and the colorbars indicate the column densities ($N_{\rm ion}/{\rm cm}^2$) for each ion. The remaining analyses are built upon the higher resolution box available at this size, `L0025N0752`. 14

2.3 The log(fractional error) found between the indicated comoving distance to pixel resolution and the highest available resolution (1.52 ckpc/pixel) as a function of $\log N_{ion}$. The 10 % error threshold is included in the figure for reference. 17

2.4 The median column density log(fractional error) of the indicated slice thickness projections in comparison to the $\Delta Z = 3.125$ cMpc projection at redshift $z = 3.53$. Five galaxies from each mass bin were chosen from the same (thin) slice of the `L0025N0752` box and statistics were determined once each pixel was allocated to the appropriate impact parameter bin; the 10 % error threshold is included in the figure for reference. 19

3.1 The column density N [cm^{-2}] 25/50/75th percentiles for all of the central galaxies in the `L0025N0752` with a specific star formation rate $\geq 10^{-11} M_{\odot}/\mathrm{yr}$ as a function of impact parameter. The box has been segmented into eight slices along the z-axis, and as a result galaxies too close to a slice boundary have been omitted.See the appendix for the column density profiles of other galaxy classes, e.g. central or non-star forming galaxies as well as a table showing how many galaxies are omitted for each class due to the slicing method. 24

3.2 The covering fraction as defined in Equation (2.4) for the galaxies in Figure 3.1. See the appendix for the covering fraction of other galaxy classes, e.g. satellite or non-star forming galaxies. 25

3.3 The metallicity, density, and temperature 25/50/75th percentiles for all of the central galaxies in the `L0025N0752` with a specific star formation rate $\geq 10^{-11} M_{\odot}/\mathrm{yr}$ as a function of impact parameter The horizontal lines in the temperature panels correspond to the collisional excitation temperatures listed in Table 1.1. See the appendix for the profiles of other galaxy classes, e.g. central or non-star forming galaxies. 26

4.1 The optical depth along the line-of-sight that passes through the galaxy in the `L0025N0752` box with ID 214610; a solid line is used to indicate its exact placement (including peculiar velocity) in redshift space. Dashed lines indicate the location (in Hubble velocity space without the incorporation of peculiar velocity) of other haloes in the EAGLE database that intersect this line-of-sight. 29

4.2 The flux $F \propto e^{-\tau}$ corresponding to the optical depths shown in Figure 4.1. 31
4.3 The composite optical depth associated with H I absorbers (25/50/75th percentiles) where each line-of-sight passing through the center of a low-mass, star-forming galaxy at $z = 3.53$ is stacked. 32
4.4 The flux assocaited with the optical depth presented in Figure 4.3. 33

5.1 The composite optical depth along lines-of-sight (25/50/75th percentiles) passing through the CGM of galaxies with the indicated attributes. About half of the total column densities along these lines-of-sight exceed $N_{H\ I} = 10^{18.5}$; when passing through the galactic center nearly all line-of-sight column densities exceed that same value. 38
5.2 The composite flux of photons (25/50/75th percentiles) with the indicated wavelength as a function of galaxy frame Hubble velocity. 39
5.3 The composite optical depths associated with Si IV absorption from lines-of-sight passing through the CGM of the galaxies in the class whose definition is informed by a recent set of observations. 40
5.4 The flux corresponding to Figure 5.3. 40
5.5 The composite optical depths associated with C IV absorption from lines-of-sight passing through the CGM of the galaxies in the class whose definition is informed by a recent set of observations. 41
5.6 The flux corresponding to Figure 5.5. 41
5.7 The composite optical depths associated with O VI absorption from lines-of-sight passing through the CGM of the galaxies in the class whose definition is informed by a recent set of observations. 42
5.8 The flux corresponding to Figure 5.7. 42
5.9 The composite optical depths associated with Ne VIII absorption from lines-of-sight passing through the CGM of the galaxies in the class whose definition is informed by a recent set of observations. 43

Version of July 29, 2019– Created July 29, 2019 - 00:59

5.10 The flux corresponding to Figure 5.9. 43

9.1 The column densities of star-forming, central galaxies the relevant annuli are stored by physical distance rather than as a fraction of the virial radius. 54
9.2 The covering fractions for galaxies represented in Figure 9.1. 54
9.3 The column densities of star-forming, satellite galaxies in physical coordinates. 55
9.4 The covering fractions for galaxies represented in Figure 9.3. 55
9.5 The column densities of non star-forming ($\dot{M}_\odot < 10^{-11} M_\odot/\mathrm{yr}$), central galaxies in physical coordinates. 56
9.6 The covering fractions for galaxies represented in Figure 9.3. 56
9.7 The column densities of non star-forming ($\dot{M}_\odot < 10^{-11} M_\odot/\mathrm{yr}$), satellite galaxies in physical coordinates. 57
9.8 The covering fractions for galaxies represented in Figure 9.7. 57
9.9 The Si IV-weighted metallicity, temperature, and density of the star-forming, satellite galaxies where the impact parameter is in physical, rather than virial, coordinates. 58
9.10 The Si IV-weighted metallicity, temperature, and density of the non-star-forming, central galaxies where the impact parameter is as a fraction of R_{vir}. 59
9.11 The Si IV-weighted metallicity, temperature, and density radial profiles of the non-star-forming, satellite galaxies in pkpc. 59
9.12 The Si IV-weighted metallicity, temperature, and density radial profiles of the star-forming, central galaxies where the impact parameter is in pkpc. 60
9.13 The Si IV-weighted metallicity, temperature, and density of the non-star-forming, central galaxies where the impact parameter is in physical coordinates. 60
9.14 The optical depth associated with photons that interact with O VI ions within the galaxies of Chapter 4. 61
9.15 The flux of photons absorbed by O VI along the line-of-sight passing through the center of each galaxy within the class discussed in Chapter 4. 62
9.16 The composite Si IV optical depth along the lines-of-sight passing through the galaxies of Chapter 4. 62

Version of July 29, 2019– Created July 29, 2019 - 00:59

9.17 The flux of photons absorbed by Si IV along the line-of-sight passing through the center of each galaxy within the class discussed in Chapter 4. 63
9.18 The composite C IV optical depth along the lines-of-sight passing through the galaxies of Chapter 4. 63
9.19 The flux of photons absorbed by C IV along the line-of-sight passing through the center of each galaxy within the class discussed in Chapter 4. 64
9.20 The composite Ne VIII optical depth along the lines-of-sight passing through the galaxies of Chapter 4. 64
9.21 The flux of photons absorbed by Ne VIII along the line-of-sight passing through the center of each galaxy within the class discussed in Chapter 4. 65

Chapter 1

Introduction

1.1 Circumgalactic Medium

1.1.1 History and Overview

Over the last sixty years the diffuse material outside of the galactic disk, now referred to as the circumgalactic medium, has gradually come into focus. A few decades before its discovery, the question of whether or not the Milky Way was the only galaxy was still an open one. Famously codified by the Shapley-Curtis debate of 1920 (see Trimble (1995) for a helpful description), it was unclear whether or not the observed non-point-like entities were small gas clouds within the Milky Way or entirely distinct galaxies. Shortly after Leavitt's discovery that Cepheid variables could be used as a standard candle, Edwin Hubble determined that the Andromeda galaxy's distance was significantly larger than the geometry of the Milky Way (Hubble (1925)), indicating that our galaxy was simply one of many.

Hubble's subsequent discovery that the recession velocities of nearby spiral nebulae were directly proportional to their distance from us indicated that the Universe itself was expanding. Given the instrumental limitations at the time astronomers were only able to observe galaxies at relatively low redshift. This gave little chance of directly observing the circumgalactic medium because it is expected to have a relatively low temperature (Tumlinson et al. (2017)). To find the CGM, there would need to be a serendipitous, sufficiently luminous background light source whose absorption spectrum would be available for observation.

Version of July 29, 2019– Created July 29, 2019 - 00:59

The first mapping of interstellar matter outside of the galactic plane that used this spectral analysis found asymmetries in the acceleration of the extraplanar ISM clouds (Münch and Zirin, 1961); Spitzer postulated the existence of a so-called 'galactic corona' and the authors determined that this theory worked well in concert with their findings. The characteristics of this corona are explained in Spitzer (1956), e.g. its ability to facilitate the growth of galactic spiral arms in the presence of a strong magnetic field. This paper provided some of the first insights into the intimate relationship between the CGM and the dynamics of the visible galaxy with which all astronomers were familiar.

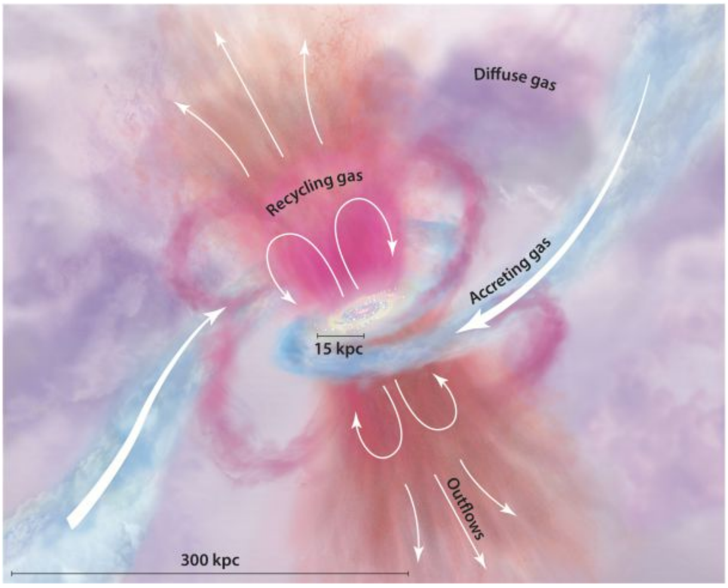

Figure 1.1: *A sketch from Tumlinson et al. (2017) of the CGM, its dynamics, and the scales on which these dynamics occur relative to the galactic disk.*

The discovery of quasars (Schmidt, 1963) allowed for the proliferation of CGM observations in galaxies besides the Milky Way. While observing a particular quasar Lynds (1971) found a surprising number of absorption lines in its spectrum. This lead to the discovery of the so-called "Lyman-alpha forest", which provides a profile of the H I distribution along a particular line-of-sight. In environments where galaxies are close together the interplay between the CGM of individual galaxies and the IGM is critical. With the development of instruments like the HST and Keck the capabilities of observing the CGM have expanded dramatically. The QSAGE survey, for example, has allowed for analysis of the CGM of low-redshift galaxies; see Bielby et al. (2019) for an example.

Tumlinson et al. (2017) provides a comprehensive review of the history of the CGM as well as open research questions being considered. Generally speaking the CGM acts as a reservoir of galactic material whose signatures can provide key insights about the galaxy's composition and evolution. More thorough observations of the gas phases of the CGM and IGM may provide a solution to the so-called missing baryon problem, in which the baryon abundance predictions proffered by cosmologists was previously out-of-sync with observations (de Graaff et al., 2019, Nicastro et al., 2018). By analyzing the ionization states of various ions within the multiphase CGM the complex dynamics within can be inferred. A particularly important component of the CGM for this thesis is the usage of metals as ”tracer particles”. Metals are generated via nucleosynthesis within large stars and supernovae. Once created in these extreme environments a significant portion of the metals is consequently ejected from the galactic plane (Emerick et al., 2018). Information regarding their abundances and velocities can then be determined using the hydrogen and metal lines within absorption spectra.

1.1.2 Open Questions

Now that it is understood that probing the deepest questions remaining in galaxy formation and evolution requires a thorough knowledge of the CGM there is wide interest in better understanding its nature. Given the inherent difficulties associated with observing the CGM many are advocating for the initiation of new missions designed to discern its various properties. The Decadal Survey on Astronomy and Astrophysics (Astro2020) is an initiative to indicate the most important topics in astronomy going into the new decade; as of July 27, 2019, there are thirteen Astro2020 white papers that discuss the circumgalactic medium available on the arXiv.

Wang et al. (2019) posits that the CGM is poorly understood in comparison to other galactic phenomena and lists (among others) the following questions: what are the metal contents of the CGM, how are they partitioned into different components (hot gas, dust, etc.), and how are these phenomena linked to external factors such as clustering and their interaction with their respective intergalactic medium environments? Their proposed solution is future multi-wavelength observations. Observations of far-UV absorption lines have been successful in probing the ISM of the Milky Way and external CGM; there is optimism that continued study of the CGM of galaxies at different redshifts could be conducted with a new far-UV space mission (Lebouteiller et al., 2019). A proposed space mission would make it possible to analyze multiple quasar sightlines such that the interplay between the CGM and ISM could be better understood. Uncovering the mechanisms behind various kinds of energetic feedback will be possible if a next-generation X-ray observatory is able to resolve feedback and gas accretion structures with temperatures exceeding $\geq 10^6$ K (Oppenheimer et al., 2019). One proposed focus is on the metal enrichment within the CGM as it provides a suitable test for cosmological simulations (Lehner et al., 2019); this is of considerable interest to this thesis as §2.3, 2.4 provide the radial profiles of several metal ions in addition to the Si IV-weighted metallicity found in EAGLE.

1.2 Cosmological Simulations

With the advent of powerful automated computers in the 20th century came a desire to simulate astronomical environments in an effort to better understand their nature and confirm that prevailing theories match observations. In the case of stellar evolution there were robust analytical models (rife with approximations such as the spherical symmetry of stars) that could be tested with computer programs. Similar efforts were made in the field of large-scale structure where the equations of fluid dynamics were used to determine how matter overdensities change with time in a non-static Universe. Understandably, these equations could only do so much to capture the possibilities associated with how immensely complicated entities like galaxy clusters evolve. A wide array of software suites have been developed to analyze these complex and non-linear environments accordingly. Several methods have been employed and it is worth discussing them in some detail.

1.2.1 EAGLE

The EAGLE project, run by the Virgo Consortium, is a suite of simulations that use hydrodynamics equations to determine the evolution of galaxies and supermassive black holes in a ΛCDM Universe (Schaye et al., 2014). Hydrodynamical simulations are considered a superior method to semi-analytic and halo-based models in some contexts due to fewer simplifying assumptions. The latter models are useful in situations where the various astrophysical phenomena present need to be disentangled, as in the case of cosmological parameter studies. Over the course of the last twenty years these simulations have improved in matching observations tremendously. This improvement is primarily attributed to better subgrid models of unresolved physics like star formation and supernovae (another connection to the field of fluid dynamics, see Premnath et al. (2009)) while improvements in the numerical techniques have also been beneficial.

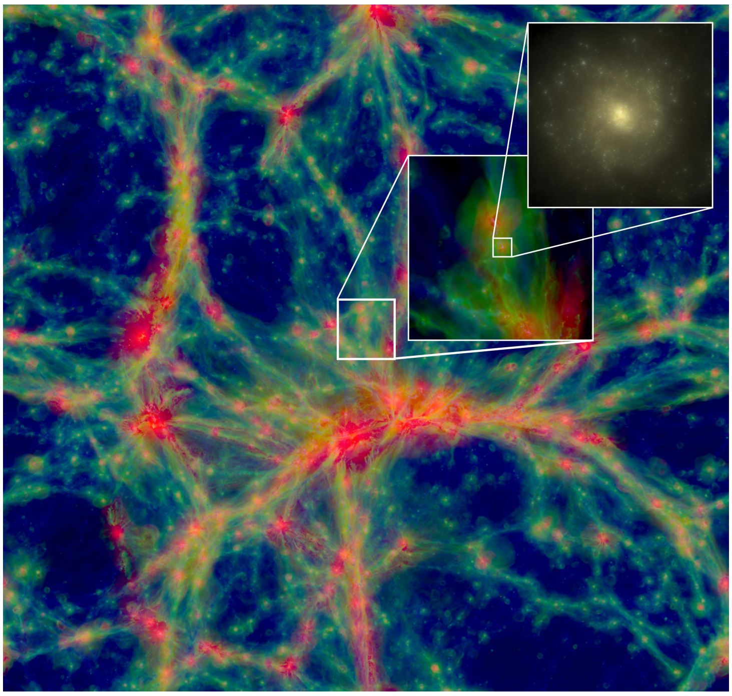

Figure 1.2: *A visualization provided in Schaye et al. (2014) of zooming in on a single galaxy found in a much larger structure (100 × 20 × 20 Mpc slice).*

The solvers used for the EAGLE simulations are a smooth particle hydrodynamics (SPH)-based solver called 'anarchy' (Crain et al., 2015, Schaller et al., 2015, Schaye et al., 2014), and tree-PM for gravity (Fukushige et al., 2005, Springel, 2005, The EAGLE team, 2017). SPH solvers are particularly popular in galaxy formation as complex boundary conditions can naturally be incorporated (Rosswog, 2009). The different subgrid models for star formation and feedback are discussed in Crain et al. (2015) where it is shown that suppressing numerical radiative losses is critical in the development of appropriately massive galaxies. Haloes are then determined using a friends-of-friends algorithm (Turner and Gott, 1976).

Analysis of the generated outputs has yielded considerable knowledge about many topics related to galaxy evolution. In Oppenheimer et al. (2016) the authors demonstrate that by using O VI absorbers as tracer particles the feedback history can be inferred on timescales comparable to the Hubble time. The cosmic spectral energy distribution of EAGLE simulated galaxies was found to be in good agreement with observations (Baes et al., 2019). While most galaxies have a correlation between their central supermassive black hole mass and stellar mass, galaxies with black holes big enough to break this correlation can be analyized using EAGLE (van Son et al., 2019). The work outlined in Cochrane et al. (2018) is especially important to this thesis as the correlation between galactic halo mass, stellar mass, and star formation rate is found to be particularly important in low mass haloes; they find that most high-SFR, low-mass galaxies in EAGLE are central galaxies in more massive dark matter haloes where the SFR is driven by an increased gas content.

1.2.2 Other Software Suites

The two most popular methods of simulating structure formation numerically are with N-body codes and fluid solvers (as EAGLE demonstrates). Some codes only model gravity while others incorporate hydrodynamics, star formation, supernovae, AGN, and gas cooling. Somerville and Davé (2015) provides a good overview of the semi-analytic models and numerical methods being pursued by the astronomical community today. To find the gravitational force on a particular particle one must solve Poisson's equation numerically; using a tree structure (see Barnes and Hut (1986)) reduces the computational complexity from $\mathrm{O}\left(n^2\right)$ when all 2-body interactions are considered to $\mathrm{O}\left(n \log n\right)$ by reducing clusters of faraway particles to their composite mass multipole moment. Additionally, the tree method has applications in gravity solvers regardless of scale. The EMERGE suite (Moster et al., 2018) utilizes an N-body solver for the simulation of galaxy evolution up to $z \sim 10$. Although the FARGO3D software suite (Benítez-Llambay and Masset, 2016) is designed for protoplanetary disks it shows that the capabilities of N-body solvers will be buoyed by further advances in GPU technology in the coming years.

While hydrodynamical solvers employing particle methods such as SPH were designed specifically for astrophysical problems, finite-difference techniques and central methods have successfully solved the compressible fluid dynamics equations in these contexts as well (LeVeque, 2011, Stone, 2007). The Enzo code (Bryan et al., 2014) uses adaptive mesh refinement to model astrophysical fluid flows that incorporate magnetohydrodyanmics (MHD) among other things and provides evidence that there is utility in combining elements of N-body and hydrodynamical solvers. ATHENA is another set of MHD codes (Stone et al., 2008) that employs adaptive mesh refinement; Dolag and Stasyszyn (2009) demonstrates that there is good agreement between this formulation and SPH. Berlok and Pfrommer (2019) explore the Kelvin-Helmholtz instability using ATHENA and indicate that this is relevant to cold flows in galaxy formation as well as cold fronts in galaxy cluster mergers.

1.3 Low-mass, Star-forming Galaxies

Our choice of focusing on analyses of the circumgalactic media surrounding low-mass, star-forming galaxies has several motivations. In an effort to understand how the CGM evolves with time we will be comparing the EAGLE simulations at various redshifts ($0 \leq z < 4$). At earlier cosmic times the galactic mass function is skewed towards the lower end of the mass régime (which makes intuitive sense as overdensities at high redshift need a considerable fraction of the Hubble time to coalesce into the structure with which we are familiar). Additionally, Figure 9 of Leitner (2012) shows the star formation histories of galaxies as a function of lookback time; at $z = 2.24$ less than 30% of today's stellar mass is present. Therefore, a one-to-one comparison of high-stellar mass galaxy characteristics is not possible for the two previously mentioned redshifts. The same paper also mentions that a star-forming galaxy is likely to have been star-

Ion	Ioniz. Energy (eV)	Ioniz. Temperature (K)	Favored CIE Temperature (K)
H I	13.6	1.58×10^5	-
Si IV	45.1	5.23×10^5	7.94×10^4
C IV	64.5	7.48×10^5	1.26×10^5
O VI	138.1	1.60×10^6	3.16×10^6
Ne VIII	239.1	2.77×10^6	6.31×10^6

Table 1.1: *The energy required from an incident photon to liberate the least bound electron from an atom with the listed ionization; see* `https://physics.nist.gov/cgi-bin/ASD/ie.pl` *for more details. The ionization temperature is the temperature at which the thermal energy $\epsilon = k_B T$ is equal to the ionization energy. The third column indicates which temperature maximizes the mass fraction of that ion while in collisional equilibrium; the corresponding H I value is not available as there is no temperature peak associated with this ion and radiative process.*

forming in the past as well, which seems to indicate that there would be few star-forming galaxies with low stellar mass at low redshifts. There are, however, effects (e.g. IGM reionization, AGN feedback, and supernova-driven winds; see Dawoodbhoy et al. (2018) and Ilbert et al. (2013)) that can suppress the star formation rate (SFR). Ilbert et al. (2013) provides a semi-analytical model that successfully replicates the observed number density of low-mass, high-SFR galaxies at the present epoch.

The temperature of the CGM, and by extension the various ionization states present in it is intimately connected to the mass of the halo via the virial theorem. The baryon budget that is observationally accounted for depends critically on the ionization state (Werk et al., 2016) so it stands to reason that the the total mass will have an effect. Table 1.1 shows the relevant ionization energies; we are primarily concerned with galaxies like those that have been associated with observed H I, C IV, and/or Si IV absorption.

Star formation has a critical role in galaxy structure and non-passive galaxies tend to have more interesting dynamical structure (Conselice, 2014). Cochrane et al. (2018) provided observational evidence that stellar mass and SFR can independently affect galaxy clustering (and via the EAGLE simulations found that these low-mass galaxies with a high SFR tend to be centered in massive dark matter haloes where the SFR is driven by an increased gas content). Quiescent galaxies evolve more rapidly in the low-mass régime (Ilbert et al., 2013) and this could be attributed to environmental effects (Martis et al., 2016).

1.4 Absorption Spectra

As mentioned in §1.1, one of the most common tools used by astronomers to determine the chemical composition of astronomical objects is an absorption spectrum. If there is a sufficiently bright background source with a well-defined emission spectrum, the composition of the intermediate space between the observer and the source can be inferred by analyzing absorption lines. The nature of gas and dust within galactic winds have been determined using absorption spectra (Heckman et al., 2000) where the illumination source is within the galaxies themselves; this material is embedded within a region where sufficiently bright sources are commonplace. A similar method called 'down-the-barrel' spectroscopy can be applied to the CGM if the embedded galaxy is sufficiently luminous (Rubin, 2017). More often, though, external objects (namely, quasars) are needed to get the CGM's absorption spectrum. The SpecWizard package, described in Theuns et al. (1998) and Schaye et al. (2003), enables us to create mock absorption spectra of this nature with the EAGLE data. By finding the frequency-dependent optical depth along a particular line-of-sight we can create a mock absorption spectum by convolving the result with a quasar emission spectrum.

1.5 Comparing Simulations to Observations

In order to ensure the analyses done on cosmological simulations are accurate comparisons to observations must be made. Sparre et al. (2018) presents a description of multiphase gas flows such that they compare nicely to observed column densities of Lyman-α haloes. The SPH code GASOLINE, which is part of the MaGICC program, was able to reproduce the O VI and H I distributions in the CGM of galaxies observed by the HST (Stinson et al., 2012). This was achieved by increasing the energy input per supernova relative to the initial model and tuning stellar feedback to match the observed relationship between stellar and total halo mass. The Milky Way's CGM is difficult to separate from the gaseous disk so Zheng et al. (2015) simulates a MW-like galaxy and finds that after correcting for path length isues the expected O VI column densities within the CGM match observations.

As mentioned in §1.1 quasars enable much more thorough observations of the CGM. The mock absorption spectra of CGM surrounding $z \sim 2$ EAGLE galaxies were compared to results from the Keck Baryonic Structure Survey, which employed QSO sightlines, in Turner et al. (2017). Simulated galaxies with halo mass $10^{12} M_{\odot}$ were found to be most similar to their observed counterparts. Figures 7 and 8 of Lau et al. (2018) show how background quasars can illuminate the CGM of foreground galaxies. Muzahid (2014) uses quasar sightlines to analyze O VI absorbers in the CGM of a galaxy at $z \sim 0.2$ and from there determines the size of the CGM and baryonic mass (assuming constant density).

1.6 Brief Overview

In Chapter 2 we present the methods with which we go about post-processing of the relevant EAGLE data. Chapter 3 (and §9.1 of the appendix) is devoted to the radial profiles of galaxy classes binned in units of pkpc as well as a fraction of the virial radius. Relevant quantities such as column densities associated with a particular ion, density, metallicty, and temperature are explored. In Chapter 4 we present mock absorption spectra found by looking along each line-of-sight associated with a galaxy of a particular class, and in Chapter 5 we move the lines-of-sight such that they intersect random regions within the CGM of a more refined galaxy class for which observations have been conducted. Chapters 6 and 7 provide qualitative discussion about how one could go about comparing the results found in this thesis to future observations in addition to a general discussion about the implications of our findings.

Chapter 2

Post-processing Preliminaries

Astronomers of all kinds are tasked with a tremendously complicated dimensionality reduction task, namely capturing the three-dimensional spatial distribution of cosmic material (either as a function of distance or Hubble recessional velocity) in a two-dimensional map. A popular method that is used throughout this thesis is a column density map, where the number of particles per unit area is counted along the dimension that is being reduced (usually along the line-of-sight). Regions with very low H I column densities were analyzed in Lockman et al. (1986) in an effort to understand the small-scale structure of the interstellar medium; such analyses are impossible when the column density values are high because the resulting spectra often incorporate additional H I sources.

Determining a column density is a well-defined task for observers but as discussed in §1.2.1 the EAGLE simulations use a hydrodynamics solver where the corresponding fluid (SPH) particle sizes are often greater than the desired map resolution. The work in this thesis uses a set of scripts written by Nastasha Wijers that reads in the EAGLE data (SPH particle locations and attributes) and provides the appropriate two-dimensional map (see Figure 1 of Wijers et al. (2019) for a sample gas surface density map and O VII/VIII column density maps).

The EAGLE data is stored in the form of databases from which information can be extracted using SQL queries. There are a number of cosmological box sizes ($L = 25, 50, 100$ cMpc) and SPH particle resolutions available to analyze. From the databases associated with that box we can glean certain information about each identified halo in the box: e.g., stellar mass, radius in which the average density exceeds $200\rho_{\mathrm{critical}}$ (which we will identify as the virial radius R_{vir}), and star formation rate. In the field of large-scale structure the critical density of the Universe ρ_{crit} plays an important role; portions of the cosmos (or indeed the entire Universe) that exceed this mass density are often expected to collapse gravitationally. It is natural then to treat the size of a galactic halo as one where the enclosed volume has a mass density that would suggest collapse has already occurred. Weak lensing studies often convolve lensing maps with a filter called a mass aperture statistic which reduces noise (Leonard et al., 2012); we chose an aperture mass statistic of 30 pkpc to define the stellar mass and specific star formation rate. A number of statistics are available in EAGLE but to ensure that this convolution did not affect our analyses we chose a filter that could be applied to each galaxy class of interest without a loss of information.

While galaxies have a radial temperature dependence $T(r)$ it is nonetheless instructive to have an order-of-magnitude estimate for the temperature of particular ions. The virial temperature of a galaxy with mean atomic weight μ is defined to be

$$T_{\mathrm{vir}} = \frac{1}{5}\frac{G\mu m_P}{k_B}\frac{M}{R_{\mathrm{vir}}}, \tag{2.1}$$

where R_{vir} is the virial radius and M is the total halo mass. In this chapter we will compare the average virial temperature of each galaxy class to the corresponding favored CIE temperatures for each available ion, which will provide insights into why a particular species' abundance may change with redshift or have low column density values when compared to other ions. Figure 2.1 shows the virial temperature for each galaxy class being considered, and shows that star-forming galaxies at high redshift often have temperatures which exceed the relevant temperatures as shown in Table 1.1. While this is a crude estimate as the temperature varies drastically within the CGM, this provides indications as to why knowing the stellar mass at high redshift is not particularly helpful when determining radial absorber abundances.

If our goal was to determine the nature of the CGM surrounding a certain type of galaxy exactly (stellar mass, star formation rate, etc.) we would need to find a column density or absorption map whose sole source

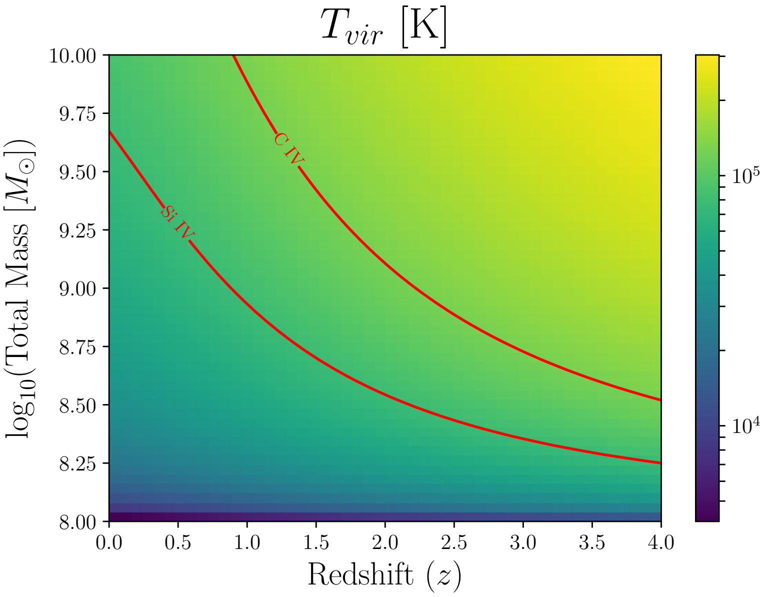

Figure 2.1: *The virial temperature as a function of total mass and redshift with contours showing the temperatures from the third column of Table 1.1. The relevant temperatures for O VI and Ne VIII exceed the virial temperature of all galaxies considered in this thesis.*

is a galaxy with the desired attributes (see Figure 2.2 for an example), repeat the mapping process for every pertinent galaxy in the box, and then run analyses on the aggregate of maps. In practice this method would be prohibitively expensive computationally as there could be $> 10^3$ haloes in the box that have a stellar mass or star formation rate in which we are interested. Additionally, this would be a poor imitation of the observation process; contamination from other objects along the line-of-sight is unavoidable so confirming the hypothetical results described in this paragraph through comparisons to observations would be dubious.

There is a method of analyzing the simulated region that would mitigate both of these concerns; we can "slice" the box perpendicular to the line-of-sight, determine column density or surface brightness projections of each slice, and then iterate through the slices to determine the projections for each halo of interest within the slice. This drastically reduces the number of times for which the projection-generating Python script has to be run; given that $\sigma \propto (N_{\text{galaxies}})^{-1/2}$ the statistics can be trusted to a much higher degree if we can analyze all of the haloes with desired parameters

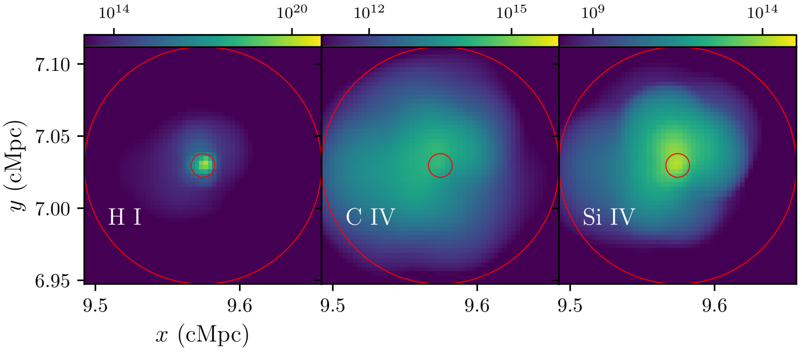

Figure 2.2: *Single halo projection of a randomly selected galaxy from the* `L0025N0376` *box at* $z = 0$ *with stellar mass* $8 < \log(M_\star/M_\odot) < 8.5$. *Contours at impact parameters* $r = 0.1R_{\rm vir}, R_{\rm vir}$ *are included for reference, and the colorbars indicate the column densities* ($N_{\rm ion}/{\rm cm}^2$) *for each ion. The remaining analyses are built upon the higher resolution box available at this size,* `L0025N0752`.

rather than a select few. Ideally this method could be used as a forward model to predict what could be found observationally but optimizing the model parameters in order to do so would be time-consuming and perhaps unnecessary.

It will be instructive to analyze the galaxies and circumgalactic media at different redshifts in order to gain qualitative insights into how the CGM evolves with time. The contents of this chapter will focus on analyzing galaxies at the present epoch as well as at redshifts $z \sim 1 - 3$. Before proceeding with the analysis of a large number of haloes we must ensure that we are using appropriate values for the resolution of our projections as well as the thickness of the box slices. These tests are run on the comparatively small $25 \times 25 \times 25$ cMpc box as we expect to find a sufficient number of haloes there with the desired stellar masses and star formation rates.

2.1 Pixel Resolution Convergence Tests

It stands to reason that the various phenomena of interest, and by extension the particular ions, would require projections with differing cross-sectional resolution. The upper limit is dictated by the storage limitations of the projections in addition to the efficacy of analyzing pixels on the order of the softening length which probes the SPH particle shape to a degree that might lead to erroneous inferences. If the projection is too coarse, on the other hand, regions of similar impact parameter but different dynamics, gas properties, etc. would be smeared. To find the optimal choice of pkpc/pixel ratio we selected a $6.25 \times 6.25 \times 6.25$ cMpc region of the high SPH resolution, 25 cMpc box that appeared to have a suitable sampling of voids and structure. We began by projecting the region along the z-axis with a $2^{14} \times 2^{14}$ pixel resolution and then reduced the resolution of the column density map with the following scheme:

$$\begin{aligned} N_{\mathrm{new}}[i,j] = \frac{1}{4}\Big(&N_{\mathrm{old}}[2i,2j] + N_{\mathrm{old}}[2i+1,2j] \\ &+ N_{\mathrm{old}}[2i,2j+1] + N_{\mathrm{old}}[2i+1,2j+1]\Big). \end{aligned} \tag{2.2}$$

Once we had the $2^n \times 2^n$ pixel projections ($n = 13, 12, 11, 10$) we computed a normalized histogram of the pixels' column densities for H I, C IV, and Si IV. In order to determine if an unacceptable amount of projection information was being altered with decreased resolution we computed the log(fractional error) $f(y,N)$ associated with a particular resolution's column density histogram $y(N)$,

$$f(y,N) \equiv \log_{10}\left(\left|\frac{y(N) - y^{\star}(N)}{y^{\star}(N)}\right|\right), \tag{2.3}$$

where $y^{\star}(N)$ is the histogram of the highest resolution available. The results for various ions at redshift $z = 0, 1, 3.53$ are shown in Figure 2.3.

The H I column density is more sensitive to a decreased resolution (see the 3rd row panels of Figure 2.3). At all three redshifts the disagreement between the highest resolution and the reduced projections exceeds 10% for column densities $\gtrsim 10^{18}$. Considering the fact that this column density value is not an unreasonable one for CGM regions around low-mass, star-forming galaxies we will have to proceed with H I projections with a resolution of 3.05 ckpc/pixel. This resolution means each pixel's physical length is $\sim 10^{-1} R_{\mathrm{vir}}$ for a $10^{10} M_{\odot}$ galaxy at redshift $z = 0$. For the metals we can operate at a much lower resolution, as the error only exceeds 10 % for the highest column density values. This could very well be attributed to the fact that there are comparatively few pixels in the projected region such that the sampling could lead to wildly varying fractional errors. In addition, high column densities associated with metals are likely to happen at very low impact parameters so an inaccurate picture of non-CGM portions of the halo should not be a concern. One mitigating concern is that at lower resolution there will be fewer pixels for a single halo which means far fewer impact parameter bins can be assembled; the computational expense is low enough that we can use the same physical distance to pixel size ratio for both H I and the metal ions we are considering. H I absorption typically comes from cooler gas found in small structures while the more energetic C IV and Si IV ions are found elsewhere; this could be one of the key elements driving the determined pixel resolution dependence.

2.2 Slice Thickness Convergence Tests

The proposed slicing method would be fairly straightforward if there were an optimal slice thickness (either in physical units or as a fraction of the entire box) such that the contamination from other objects along the same line-of-sight matched that which is found in observations. This optimal slice thickness would also place an upper limit on the number of projections that have to be computed. To determine if such an optimal slice thickness could transcend varying values of stellar mass and apply to ions of varying ionization energies we ran a convergence test for galaxies randomly selected from five total mass bins. We selected five galaxies from each bin contained in a single $\Delta Z = 3.125$ cMpc slice and then combined projections to indicate what the result would be for slice thicknesses $\Delta Z = 6.25, 12.5, 25$ cMpc. Figure 2.4 shows the fractional difference between the thinnest slice projection and the consequent slice combinations.

The error generally increases with increasing impact parameter (especially for H I) which should not be a surprising result, as the column densities at $\gtrsim 0.5R_{\rm vir}$ will be very low for the single halo projection and introducing material from other objects along the line-of-sight will provide the bulk of the contamination. The cosmological principle would suggest that these contaminating objects do not have a preferred azimuthal coordinate; if the slices are a good model we should be able to infer whether EAGLE properly captures the properties of contaminating objects for these mock

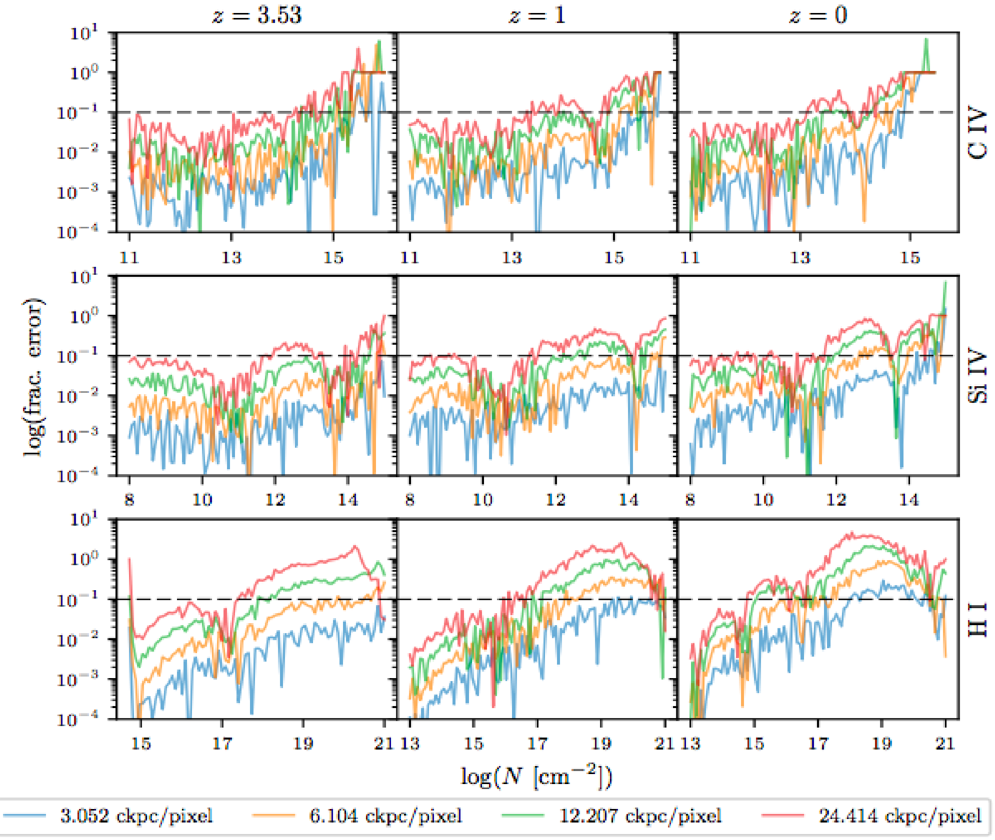

Figure 2.3: *The* log*(fractional error) found between the indicated comoving distance to pixel resolution and the highest available resolution (1.52 ckpc/pixel) as a function of* $\log N_{ion}$*. The 10 % error threshold is included in the figure for reference.*

observations.

The column density values used to compute the fractional errors shown in Figure 2.4 are the median value of the pixels with the indicated impact parameter. Different impact parameters could be affected by things such as smooth absorption over large lengths and foreground/background objects so it was worth noting that this test is not exhaustive and should not indicate an ideal slice thickness that best serves our purposes of comparing the results derived from the EAGLE simulations to what has been observed.

2.3 Methods of Sampling the Cosmological Box

We are concerned with finding quantities as a function of impact parameter starting from a column density map and a list of galaxies; this involves converting from pixel to physical units and binning together each pixel with a particular impact parameter. Once this is achieved we can find statistics concerning a particular impact parameter bin (median, 90th percentile, etc.) or determine the covering fraction, which is defined in the following way:

$$F(N_{th}, b) \equiv \frac{n_{\text{pixels}}(N > N_{th}, b)}{\sum n_{\text{pixels}}(b)}, \tag{2.4}$$

where $n_{\text{pixels}}(N > N_{th}, b)$ is the number of pixels with impact parameter b whose column density N exceeds a threshold column density value N_{th}. Covering fractions are a helpful tool when comparing to observations (see Muzahid et al. (2016) for an example) as telescopes are often unable to resolve column densities below a certain value; as Equation (2.4) demonstrates, this limitation can be incorporated in computational research quite nicely.

If we are to proceed with the slicing method to find projections for all of the relevant haloes in the box we must determine a suitable method of doing so. With only one slice (namely, the entire box) there could be an unrealistic amount of contamination from other haloes along the same line-of-sight. Conversely, using a number of slices such that the slice thickness is $\lesssim \langle R_{\text{vir}} \rangle$ making the projections would become perhaps prohibitively expensive, a great number of pixels would be computed without being used, and we would not be able to compare to observations in a meaningful way.

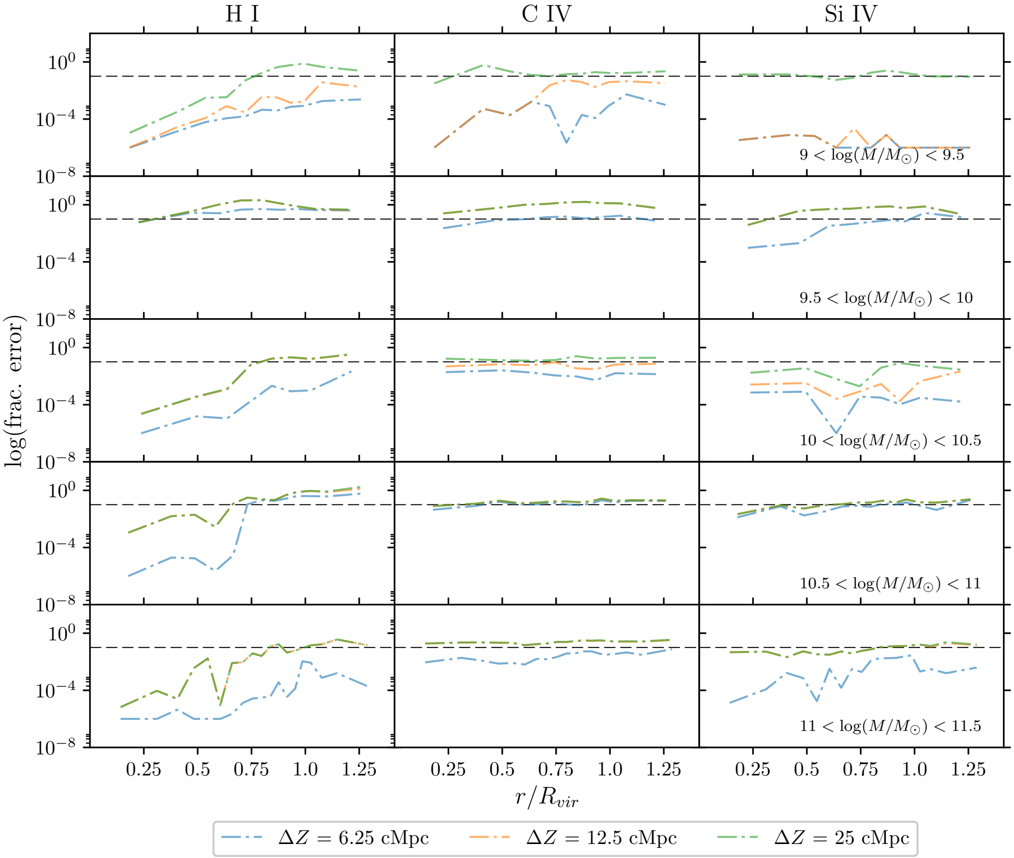

Figure 2.4: *The median column density* $\log$*(fractional error) of the indicated slice thickness projections in comparison to the* $\Delta Z = 3.125$ *cMpc projection at redshift* $z = 3.53$*. Five galaxies from each mass bin were chosen from the same (thin) slice of the* `L0025N0752` *box and statistics were determined once each pixel was allocated to the appropriate impact parameter bin; the 10 % error threshold is included in the figure for reference.*

Chapter 3

Radial Profiles of EAGLE Galaxies

3.1 H I

For the analyses in this chapter we chose to use 8 slices of the 25 cMpc, high-SPH particle resolution cosmological box in an effort to get a more refined sense of the circumgalactic ion distributions. One complicating factor is that some galaxies might be too close to a slice boundary such that material gravitationally bound to that particular halo might be in another slice. There are several ways in which this issue could be mitigated: allow for the inclusion of an additional slice in the event a galaxy is contained within multiple slices, include the outputs from a fixed number of neighboring slices whose z_{center} values are closest to that of the halo, or simply omit galaxies from the analysis that are split up into multiple slices. The first possibility would make certain galaxies more important than others as thicker projections will invariably have higher column densities and covering fractions. The ideal method would come from slicing the box such that each slice had a thickness $\sim \langle R_{\text{vir}} \rangle$ and then included a number of slices N such that a projection whose depth was equal to $\frac{\Delta Z}{N} \times \langle R_{\text{vir}} \rangle$ would capture the relevant galaxies as well as the expected amount of contamination found in observations. In practice, however, this would defeat the purpose of the slicing method as a significant portion of data generated from the projection script would be thrown away and it would behoove us to restructure the code in such a way that the projections are found of each relevant halo individually.

The EAGLE simulations employ periodic boundary conditions (as do most hydrodynamics solvers) so we can include these galaxies by incorporating a contingency into the script that takes the pixels from the appropriate projections even if they are on the other side of the box in any of the x, y, or z directions.

Neutral hydrogen is one of the primary absorbers of interest when analyzing the dynamics of the CGM. Cen et al. (1994) shows that low H I column density values originate from Zel'dovich pancake-like regions (flat, large-scale structures that arise from density perturbations, see Zel'dovich (1970)) while high H I column density values are indicative of shocked gas still undergoing the cooling process. These results were derived from semi-analytic modelling of a ΛCDM Universe similar to EAGLE.

The bottom row of panels in Figures 3.1 and 3.2 show the H I column density and covering fractions at redshifts $z = 0, 1, 3.53$ with slice thickness $\Delta Z = 3.125$ cMpc. At each redshift the amount of H I is correlated with the total mass of the galaxy class (except for the lowest mass bin when it is present at $z = 1, 3.53$), but this stratification becomes less important at high impact parameter. The H I values drop by several orders of magnitude with decreasing redshift; whether or not this is attributable to a completed cooling process is beyond the scope of this thesis as it would require absorption spectra for a wide range of galaxy classes at different redshifts.

It has been shown that the gas density profiles of the CGM are self-similar (Pallottini et al., 2014). In the same paper an H I column density function dependent on impact parameter (assuming spherical symmetry) is proffered:

$$N_{H\ I}(b) = \frac{2}{m_H} \int_b^{\ell_{max}} \rho_{PP}\, x_{H\ I} \frac{r}{\sqrt{r^2 - b^2}} \mathrm{d}r, \tag{3.1}$$

where the gas density profile ρ_{PP} is self-similar, $x_{H\ I}$ is the ion fraction, and $\ell_{max} = \sqrt{b^2 + (\Delta v/H)^2}$ encapsulates the velocity window from observations in a similar fashion to our slicing method. Figure 2 of that paper, which plots the column density for varying halo mass, qualitatively matches the findings provided here.

Observations of the H I present in the CGM of galaxies low redshift have been difficult to accomplish; Pisano et al. (2019) discusses current progress in this effort. The covering fraction of AMIGA data (with $N_{th} =$

$10^{17.6}$) shows strong suppression at intermediate-to-high impact parameter, although not to the degree shown in the bottom panels of Figure 3.2. If we were to determine a galaxy's total mass using an incomplete covering fraction it appears that for H I it be best to sample small impact parameters at low-to-intermediate redshift and large impact parameters at high redshift. The most enigmatic profile is that of the lowest total mass galaxy class, whose H I covering fractions exceed the next two most massive classes until $\sim 0.5 R_{\text{vir}}$.

3.2 Si IV and C IV

The top two rows of panels in Figures 3.1 and 3.2 show that there are few distinguishing characteristics between the profiles associated with Si IV and C IV. The latter is more ubiquitous by about an order of magnitude at all redshifts and the covering fraction profiles are qualitatively very similar at all redshifts. The decrease in column density is more gradual with decreasing impact parameter, especially at higher redshifts. Stratification by total mass is more clear with the exception of at low mass and high impact parameter for redshift $z \sim 1$, where again the lowest mass galaxy class displays some peculiar behavior by maintaining almost a constant metal abundance at $r \gtrsim 0.75 R_{\text{vir}}$.

Oppenheimer et al. (2018) partitions the CGM into an inner and outer region whose boundary is the sphere with radius $0.5 R_{\text{vir}}$, and the features of Figure 2 of that paper qualitatively match those shown in Figure 9.1 in the appendix. It is worth noting that their analyses were at slightly higher redshifts and total masses; additionally, the authors of that paper employ what are called zoom simulations. As evidenced by Figure 2.2 the projections with which we are working are fairly coarse; by using the initial parameters (e.g., primordial power spectrum) of a very small region within a particular cosmological box the corresponding resolution is considerably higher.

Zoom simulations with other sets of codes have yielded interesting information regarding the outflows and cold streams of metals at $z \sim 3$ (Shen et al., 2013). While profiles are not provided the zoom simulations indicate that column densities are spherically asymmetric, especially in the case of H I and Si IV. Figures 3a and 3b of that paper corroborate our

Version of July 29, 2019– Created July 29, 2019 - 00:59

findings that some column densities are nearly constant until very high impact parameters at high redshift (see the top and middle left panels of 3.1.

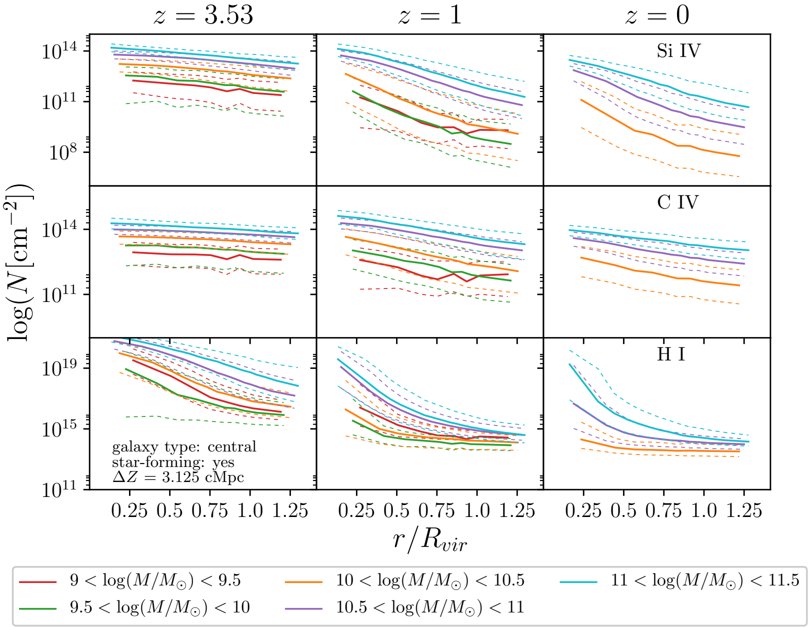

Figure 3.1: *The column density* $N\,[\mathrm{cm}^{-2}]$ *25/50/75th percentiles for all of the central galaxies in the* `L0025N0752` *with a specific star formation rate* $\geq 10^{-11} M_\odot/yr$ *as a function of impact parameter. The box has been segmented into eight slices along the* z*-axis, and as a result galaxies too close to a slice boundary have been omitted.See the appendix for the column density profiles of other galaxy classes, e.g. central or non-star forming galaxies as well as a table showing how many galaxies are omitted for each class due to the slicing method.*

3.3 Density, Temperature, and Metallicity

There are certain local quantities that would provide key insights into the nature of the CGM, but measuring such things through line-of-sight measurements is effectively meaningless. For example, all of the temperatures along a line-of-sight would at best be a composite measure rather than provide any information about the temperature at various regions. To probe these quantities we need a bulk quantity for which we can directly measure total values along the line-of-sight like column density. With this idea

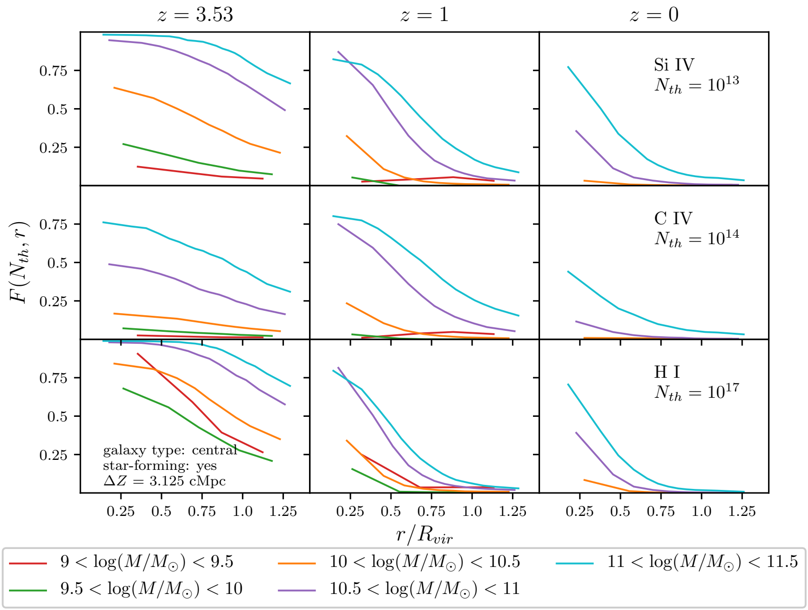

Figure 3.2: *The covering fraction as defined in Equation* (2.4) *for the galaxies in Figure 3.1. See the appendix for the covering fraction of other galaxy classes, e.g. satellite or non-star forming galaxies.*

in mind, the EAGLE data-to-projection script mentioned in the beginning of Chapter 2 is capable of measuring *ion-weighted* local quantities like temperature. We chose to weight them with S IV as it is fairly ubiquitous for all galaxy classes at all redshifts and impact parameters (as shown in the top three panels of Figure 3.1.

The top three panels of Figure 3.3 show that the metallicity increases with time, which makes intuitive sense given stellar enrichment. Unlike column densities the metallicities maintain the same order of magnitude with increasing impact parameter. Figure 9.10 in the appendix shows that metallicity does increase with time regardless of star formation histories but the values of the metallicities themselves are critically dependent on this process. The middle panels suggest that distinguishing galaxy class by temperature a difficult proposition. At no point in time or for any low-mass galaxy class does the median temperature exceed the collisional excitiation temperatures for the metals in which we have been interested, but the higher percentiles could exceed these thresholds to some degree, especially at low-to-intermediate redshift. The Si IV-weighted temperature is nearly constant across cosmic time; this would suggest that various in-

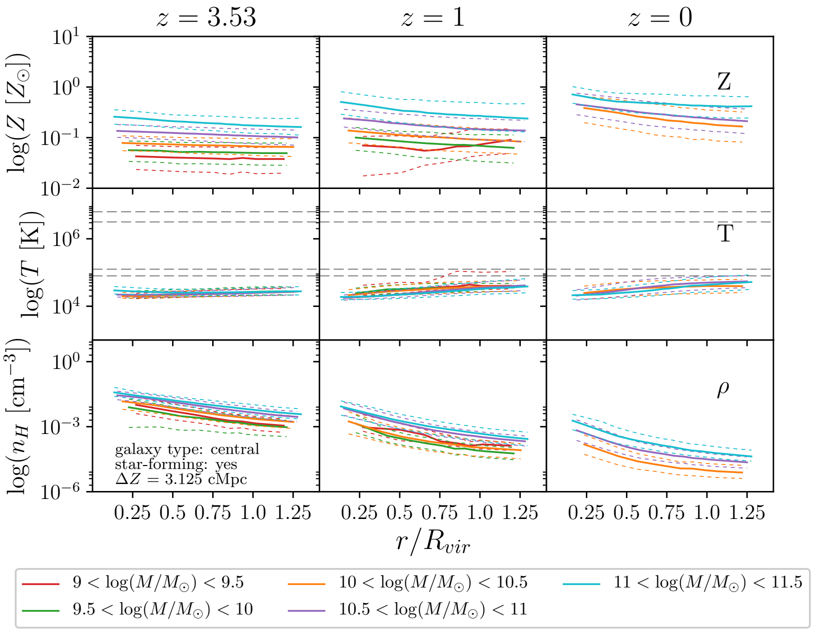

Figure 3.3: *The metallicity, density, and temperature 25/50/75th percentiles for all of the central galaxies in the* `L0025N0752` *with a specific star formation rate* $\geq 10^{-11} M_\odot/yr$ *as a function of impact parameter The horizontal lines in the temperature panels correspond to the collisional excitation temperatures listed in Table 1.1. See the appendix for the profiles of other galaxy classes, e.g. central or non-star forming galaxies.*

ternal processes are negligible contributors to the maintenance of the cosmic thermostat; instead it seems reasonable that least for Si IV weighted temperatures a global galactic measurement (perhaps even the virial temperature T_{vir}) would be a suitable approximation. Ions tend to be biased temperature probes; as a result, this sort of information typically needs to be supplemented by column density profiles as the abundances of particular ions can provide more information about the gas phases present in the CGM. Of these local quantities it is unsurprising that the density profiles are most similar to that of the column densities. It is worth noting, however, that these galaxies have very similar density profiles when binned by virial radius; this would suggest that low-mass, star-forming galaxies are homologous in this specific context.

Chapter 4

The Precursors to Mock Absorption Spectra with EAGLE Data

The content of the previous chapter and this one are closely connected, as the properties (e.g., density) and ion abundances present along a particular line-of-sight inform the extent to which an external object's light can pass through the intermediate material. A quantitative measure relevant to this sort of analysis is the optical depth, which is defined to be

$$\tau(\nu_{obs}) = \int_0^{z_{emit}} \sigma\left(\nu_{obs}(1+z)\right)\, n_{\rm ion}(z) \left|\frac{\mathrm{d}\lambda}{\mathrm{d}z}\right| \mathrm{d}z, \tag{4.1}$$

where z_{emit} is the redshift at which the emitting object is observed, $\frac{\mathrm{d}\lambda}{\mathrm{d}z}$ is the derivative of the proper distance to the emitting object with respect to redshift, ν_{obs} is the frequency at which the light associated with a particular ion is observed, and $\sigma\left(\nu = \nu_{obs}(1+z)\right)$ is the frequency-dependent scattering cross section (Kitchin, 1987). The associated flux is

$$F(\nu_{obs}) = F_c(\nu_{obs})\mathrm{e}^{-\tau(\nu_{obs})}, \tag{4.2}$$

where F_c is the continuuum flux at that frequency. At first glance Equations (4.1) and (4.2) provide an intuitive relation between optical depth/flux and the associated column density; however, the process of computing the cross-section term necessitates a thorough understanding of how a photon wavepacket is scattered once it interacts with an ion (see Chapter 7 of Sakurai et al. (1995) for more details). For the analyses presented in Chapters 3 and 4 that are dependent on this optical depth calculation we use the SpecWizard package. Upon providing a simulation (EAGLE, `L0025N0752`), a list of ions (H I, Si IV, C IV, O VI, Ne VIII), and a number of lines-of-sight we are given the relevant optical depth profiles through the box as a function of rest-frame Hubble velocity.

The SpecWizard package reads in particles from the EAGLE data along the line-of-sight, determines the locations of the relevant ions, and computes the number of ions using the ion fractions available from density and temperature tables. From this set of information a position space ion density spectrum can be extracted. The quantum mechanical nature of the absorption process is codified with the wavelength and oscillator strength associated with a particular ion, the latter being a measure of the probability that a certain electron orbital transition will occur (Robinson, 1996). Combining the ion population information with the quantifiable description of how absorption occurs, including self-shielding (Rahmati et al., 2013), for that ion produces the optical depth along the line-of-sight.

4.1 Flux and Optical Depth Along a Line-of-sight

We began the analyses of §4.1 and 4.2 by selecting all of the galaxies in the `L0025N0752` box at redshift $z = 3.53$ with total masses $9 < \log(M/M_\odot <$ 9.5 and specific SFRs exceeding $10^{-11} M_\odot/yr$. This yielded 1328 galaxies, and we developed a script that would generate line-of-sight coordinates in the xy plane as a fraction of the box size. These coordinates were pointed directly through the center of each galaxy, so the consequent figures are representative of the galactic centers rather than the CGM itself; in Chapter 5 we will discuss ways of mimicking the line-of-sight determination process used in observations of the CGM. In addition to computing quantities such as optical depth and flux along each line-of-sight SpecWizard determines the peculiar velocity at each point, defined to be the movement independent of the Hubble flow:

$$\mathbf{v}_{pec} = \dot{\mathbf{r}} - H\mathbf{r}, \tag{4.3}$$

where $\mathbf{r}$ is the point's proper coordinate. These velocities distort the observed spatial distribution of material (Kaiser, 1987). SpecWizard computes the gas peculiar velocity along the line-of-sight to account for this distortion, and while it would be interesting to see the absorption spectra with this effect turned off it is beyond the scope of this thesis. In order to indicate where the galaxies through which this line-of-sight passes we must find their respective coordinates in position space, account for Hubble flow, and incorporate the peculiar velocity values that have been computed for that location along the line-of-sight.

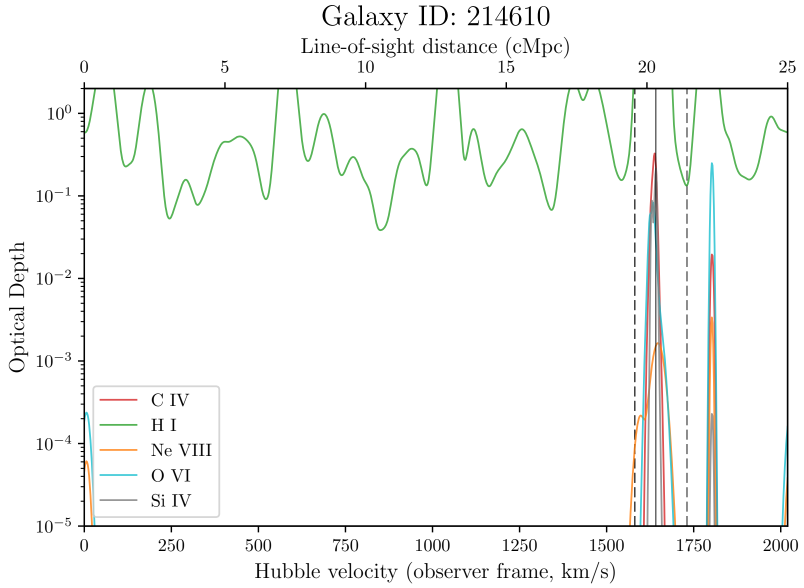

Figure 4.1: *The optical depth along the line-of-sight that passes through the galaxy in the* `L0025N0752` *box with ID 214610; a solid line is used to indicate its exact placement (including peculiar velocity) in redshift space. Dashed lines indicate the location (in Hubble velocity space without the incorporation of peculiar velocity) of other haloes in the EAGLE database that intersect this line-of-sight.*

Figure 4.1 shows the optical depth associated with five ions along the line-of-sight passing exactly through the center of a low-mass, star-forming galaxy at high redshift (by our standards). Along a considerable portion of the line-of-sight the H I optical depth exceeds that of the definition of a stellar photosphere, $\tau = 2/3$. The presence of additional (possibly extraneous) galaxies along the line-of-sight is correlated with asymmetries in the optical depth about the central galaxy in redshift space.

The corresponding fluxes, as shown in Figure 4.2, corroborate the opacity associated with H I absorption and strong dependence on galaxies along the line-of-sight for metal absorption. If Equation 4.1 is evaluated assuming no peculiar velocities then it can be shown that

$$\tau(\nu_{obs}) \propto n_{H\ I}(z). \tag{4.4}$$

In turn the flux is proportional to $\exp\left(-n_{H\ I}(z)\right)$; Figure 4.2 indicates that there are H I clouds along the line-of-sight that are entirely independent from the relevant galaxies. This suppression of background Ly-α emission is not thorough enough to be considered the manifestation of the Gunn-Peterson trough within the relevant EAGLE simulation, where the comparatively low abundance of neutral hydrogen in the intergalactic medium would indicate that a reionization epoch occurred at some redshift between the one we are considering ($z = 3.53$) and recombination ($z \sim 1100$). Although the sources of UV and X-ray radiation to reionize the IGM have not yet been precisely determined it has been shown that Population II/III stars, as well as quasars, are suitable candidates (Baek et al., 2010).

The fluxes corresponding to metal lines are comparatively high and almost exactly 1 for regions further than 50 km/s from a galaxy in redshift space. The favored collisional ionization temperatures for these species are greater than 70000 K, which is uncommon for material not associated with virialized structures. Rather surprisingly it appears the strongest absorber associated with the galaxy with which the line-of-sight is centered is C IV, while O VI dominates for the galaxy whose redshift distance separation is 250 km/s from the primary galaxy of interest. It is likely that these differences in absorber strengths are attributable to galactic attributes such as total mass and specific star formation rate.

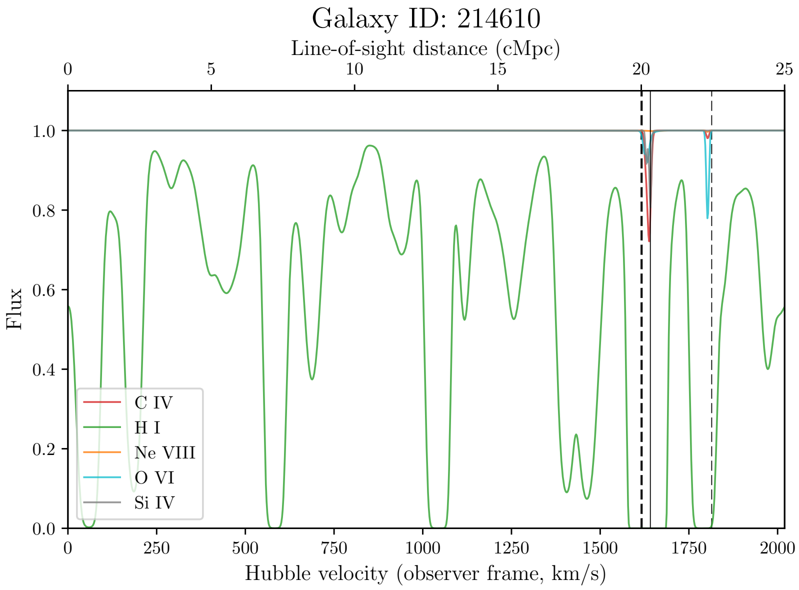

Figure 4.2: *The flux $F \propto \mathrm{e}^{-\tau}$ corresponding to the optical depths shown in Figure 4.1.*

4.2 Composite Absorption Profiles

The contents of the previous section were a precursor to the composite optical depth/flux profiles that will serve as our primary tool for comparing the EAGLE simulations to real observations. Each line-of-sight begins at the observer (0 km/s in redshift space) and continues on through the entire box. To find optical depth/flux statistics as a function of *galaxy frame* Hubble velocity we had to manipulate the spectra such that each one was centered on the galaxy in redshift space. This was achieved by converting the galaxy's total velocity $\dot{\mathbf{r}}$ into redshift space coordinates and "rolling" (borrowing from the parlance of the `numpy` library) the spectrum arrays such that they were centered on the galaxy used to generate the line-of-sight. Once each array had been rolled the statistics of each element bin were computed. Another way of expressing this idea is by imagining each row of a 2D NumPy array corresponds to a particular line-of-sight spectrum of length N and each column a galaxy frame Hubble velocity value; the following values are plotted in Figures 4.3 and 4.4:

```
np.percentile(spectra[:,i], x),
```

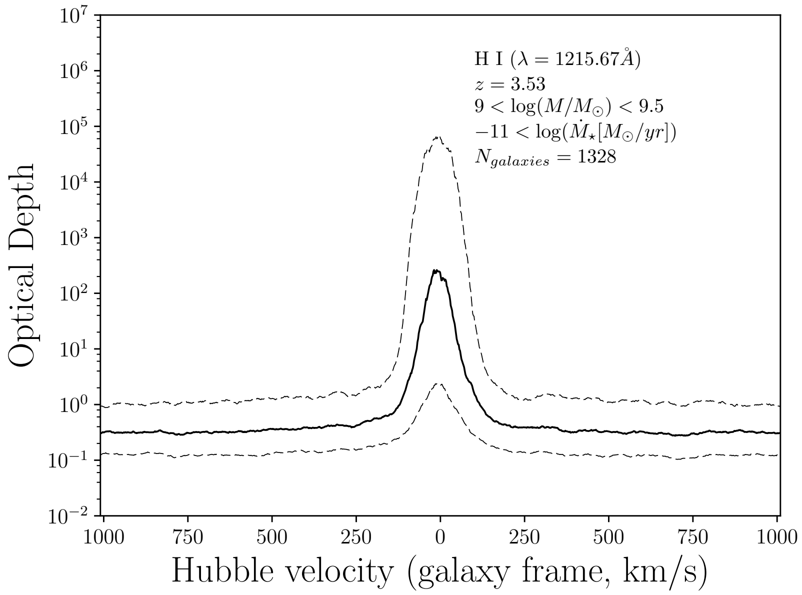

Figure 4.3: *The composite optical depth associated with H I absorbers (25/50/75th percentiles) where each line-of-sight passing through the center of a low-mass, star-forming galaxy at* $z = 3.53$ *is stacked.*

where $x = 25, 50, 75$ and $i \in [0, N - 1]$. The corresponding metal line profiles can be found in the appendix. At separations of 100 km/s in redshift space the galaxy absorbs nearly all of the incident radiation associated with H I. At more disparate positions along the line-of-sight the H I flux settles into a median value of ~ 0.75; this is an indicator of how H I is absorbed by the intermediate material within the EAGLE simulations rather than a set of damping wings (phenomenon where high column densities yield a saturated aborption line and Lorentz broadening increases absorption outside of the main line, (Gunn and Peterson, 1965)).

Of all of the metals we considered, O VI was the strongest absorber of the photons passing through this set of EAGLE galaxies. This absorption, however, was nearly negligible; the largest median optical depth was $\tau \sim 10^{-3}$, which is several orders of magnitude below standard definitions of opaque material. Given the collisional ionization temperatures we should suspect that the strongest metal absorber would either be Si IV or C IV. These lines-of-sight pass directly through the center of each galaxy so perhaps the densities and temperatures through which these photons pass favor different photoatomic reactions.

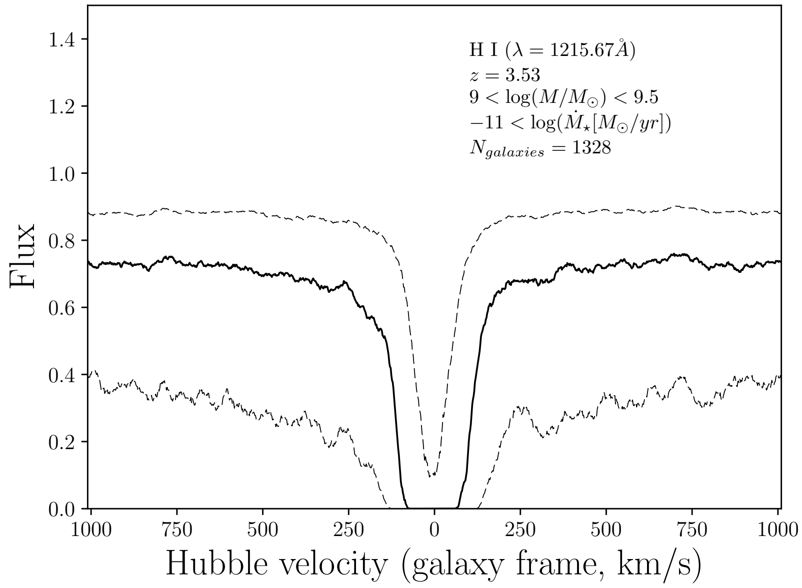

Figure 4.4: *The flux assocaited with the optical depth presented in Figure 4.3.*

Chapter 5

Comparison to Observations

5.1 Status of Comparing CGM Simulations to Observations

Methods of observing the CGM are robust and varied, so our analyses should mimic these practices while simultaneously achieving improvements due to the nature of having a large suite of simulations wherever possible. Given the limitations of observing material on the periphery of galaxies as mentioned in §1.1.1, it is critical to complement these studies with corresponding results from simulations.

The "stacking" method employed by observers of the CGM was implicitly introduced in §4.2. By combining the spectroscopic contributions from each galaxy within a collection of hundreds or thousands with similar parameters, statistical noise can be effectively erased. Figure 10 in Steidel et al. (2010) divides the galaxy sample into two mass bins (total mass either above or below $3.7 \times 10^{10} M_{\odot}$) and plots the normalized intensity as a function of galaxy frame Hubble velocity; while qualitatively similar to the results presented in this chapter, their profiles are considerably more asymmetric about $v_{Hubble} = 0$ km/s and have non-negligible absorption features for all of the ions, not just H I.

Among the benefits of using the EAGLE simulations for comparisons to observations, we are not limited by saturation effects or comparatively poor statistics stemming from a sample of few galaxies. For column densities $\log(N_{H\ I}) \sim 18$ the entire Lyman series is saturated (Tumlinson et al., 2017); this implies that observed stacks of pencil beams passing through a set of galactic centers would not be able to produce Figures 4.3 and 4.4. The multiphase nature of the CGM was determined using O VI and C IV absorbers in Rudie et al. (2019), but the results were derived from only eight $\sim L^{\star}$ galaxies at $z \sim 2$; the small sample was mitigated by using multiple lines-of-sight (130 in total) for each galaxy in the sample. The results presented in §5.2 use one line-of-sight for ≥ 200 galaxies of a particular class. A similar study found that O VI absorbers were a suitable tracer of outflowing and accreting CGM gas and did so with observations of O VI within 29 galaxy environments in a fairly narrow redshift band (Nielsen et al., 2017). Chen (2012) posits that the CGM has not changed dramatically from $z \sim 0 - 2$, and they mitigated this sampling issue by analyzing a collection of five different galaxy observation samples from the literature.

5.2 Circmgalactic Media of EAGLE Galaxies Ready For Direct Comparsion

In Chapter 4 we found the (x, y) coordinates from the EAGLE database for each of the low-mass, star-forming central galaxies at $z = 3.53$ in the `L0025N0752` box (13th row of Table 9.1). From that list of ordered pairs we computed line-of-sight measurements along the z-direction and presented an example of a single line-of-sight optical depth/flux profile passing through a galactic center and the resulting composite profiles.

Adjustments needed to be made in order to more accurately mimic the CGM observation process. We needed to collect precise measurements of the attributes associated with the CGM (rather than the galactic centers) and the galaxy class definition needed to be sharpened such that we could compare more directly to an existing set of observations. The new galaxy class had the folowing total masses and star formation rates:

$$10^{9.5} M_{\odot} \leq M_{\star} \leq 10^{11.5} M_{\odot}, \tag{5.1}$$

$$10^{-0.65} M_{\odot}/\mathrm{yr} \leq \dot{M}_{\star} \leq 10^{0.74} M_{\odot}/\mathrm{yr}. \tag{5.2}$$

From observations the specific star formation rate of a particular galaxy is well understood but the total mass (especially at higher redshift) is susceptible to fairly large uncertainties, which is incorporated into the definition of our galaxy class. To achieve our goal of creating mock absorption spectra of the CGM surrounding low-mass, star-forming galaxies we needed to adjust our line-of-sight determination algorithm. Rather than choosing the coordinates given in the EAGLE database, we incorporated random number generators to create a new ordered pair $(x', y') = (x + r\cos\theta, y + r\sin\theta)$, where the polar coordinates r, θ were determined using a random number generator that provided values in the following ranges.

$$r \in [20, 320)\,\text{pkpc}, \tag{5.3}$$

$$\theta \in [0, 2\pi). \tag{5.4}$$

We should point out that our sampling scheme was biased towards small impact parameters; a uniform polar coordinate sample would distribute lines-of-sight evenly through impact parameter slices with area $2\pi r \Delta r$. This was intentional; observations tend to be focused on the circumgalactic regions closer to the galactic disk and as a consequence we incorporated this trend into our line-of-sight generator.

From the EAGLE database we found 213 galaxies in the `L0025N0752` box at redshift $z = 3.53$ that belonged to this galaxy class; their composite optical depth is shown in Figure 5.1. At galaxy frame Hubble velocities of greater than 500 km/s one the optical depth is similar to the more broadly defined galaxy class (see 4.3). As expected the peak optical depths are smaller than in the Chapter 4 case as the lines-of-sight are passing through the CGM rather than the galactic center which presumably has a higher H I absorber density.

The corresponding flux of $\lambda = 1215.67 \mathring{A}$ photons is shown in Figure 5.2. The median optical depth of the CGM for this ion is about an order of magnitude larger than in the galactic center, which explains why a negligible number of these photons avoid absorption for galaxy frame Hubble velocites of less than 50 km/s. This would suggest that the ion fraction of neutral hydrogen is higher in the CGM; this makes intuitive sense as hydrogen atoms are more likely to be ionized in the density and temperature régimes associated with the centers of galaxies. It is possible that

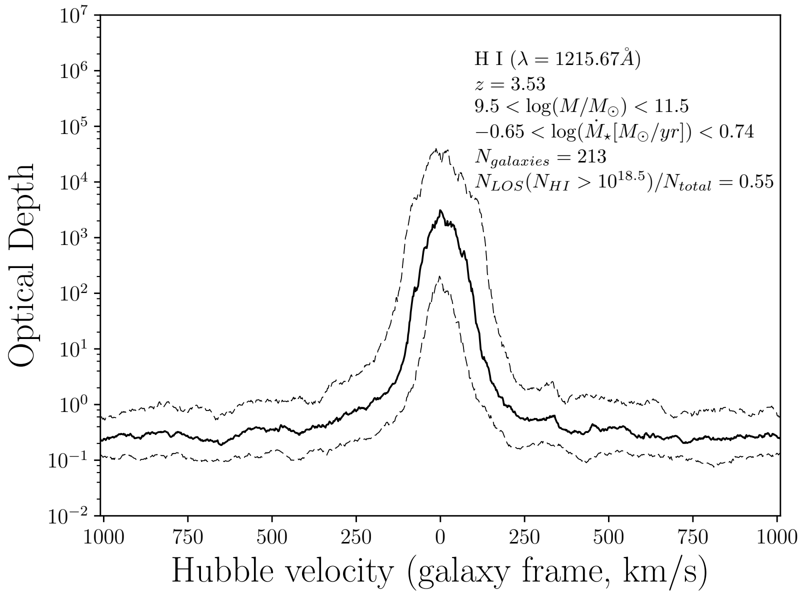

Figure 5.1: *The composite optical depth along lines-of-sight (25/50/75th percentiles) passing through the CGM of galaxies with the indicated attributes. About half of the total column densities along these lines-of-sight exceed* $N_{H\ I} = 10^{18.5}$*; when passing through the galactic center nearly all line-of-sight column densities exceed that same value.*

the different galaxy class definitions could be partially responsible for this discrepancy; the total mass range is larger and Figure 3.2 shows that H I abundance at high redshift is dependent on both total mass and impact parameter. The change in specific star formation rate definition would require a deep connection between star formation and neutral hydrogen abundances in the CGM.

Figures 5.3 through 5.10 show the absorption spectra for several metal absorbers. The most ubiquitous of these ions are C IV and O VI according to the medians shown in Figures 5.6 and 5.8; Si IV and Ne VIII are not nearly as strong but the flux at small galaxy frame Hubble velocities is lower than when the lines-of-sight pass through the galactic centers. It appears that there is a correlation between the broadness of the optical depth peak and the associated energies listed in Table 1.1. This may be related to the transition from collisional ionization being the dominant photoatomic mechanism in the CGM to other processes closer to the galactic center. The optical depth associated with Ne VIII absorption, for example, does

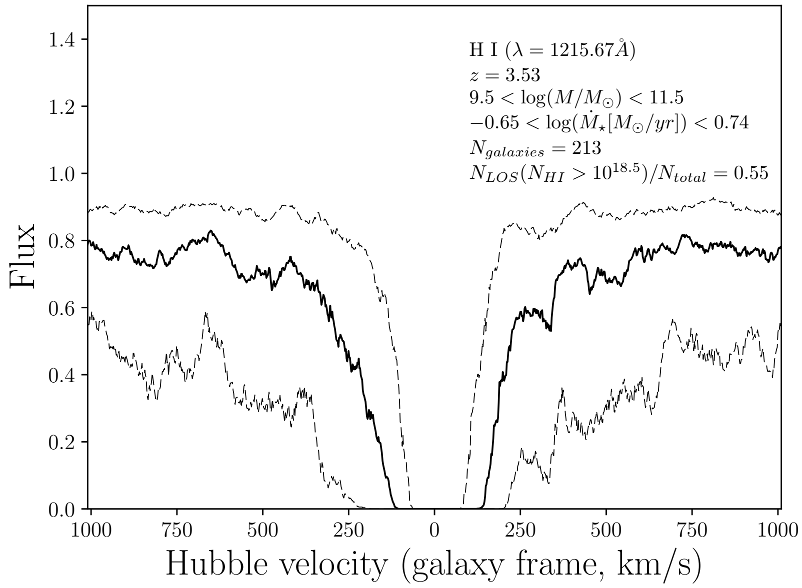

Figure 5.2: *The composite flux of photons (25/50/75th percentiles) with the indicated wavelength as a function of galaxy frame Hubble velocity.*

not change very much as the line-of-sight passes through the CGM because the favored CIE (see Table 1.1) is too high for collisional ionization to be an important feature for that particular ion in this region. Figure 9.20 shows that when the lines-of-sight pass through the galactic center the Ne VIII absorption is considerably broader, indicating that the location of the line-of-sight is critical in understanding the ion absorption line widths.

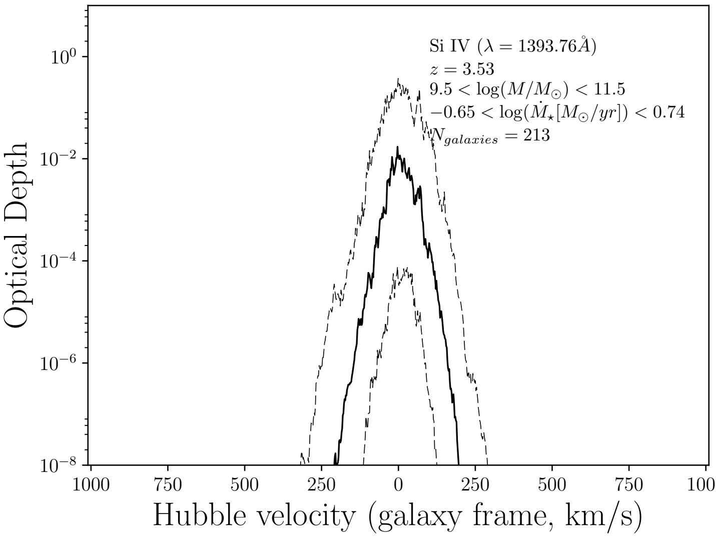

Figure 5.3: *The composite optical depths associated with Si IV absorption from lines-of-sight passing through the CGM of the galaxies in the class whose definition is informed by a recent set of observations.*

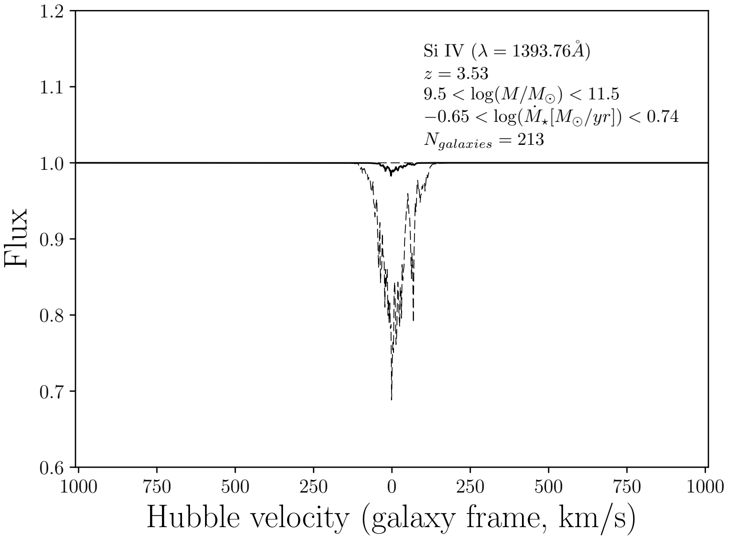

Figure 5.4: *The flux corresponding to Figure 5.3.*

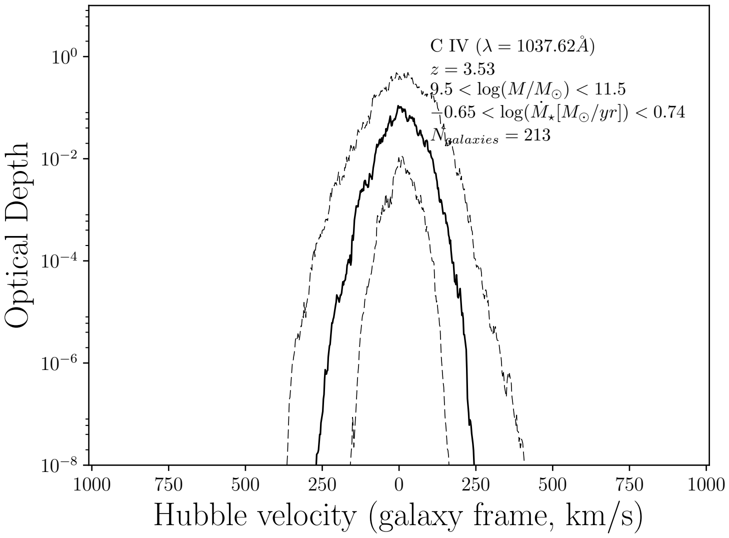

Figure 5.5: *The composite optical depths associated with C IV absorption from lines-of-sight passing through the CGM of the galaxies in the class whose definition is informed by a recent set of observations.*

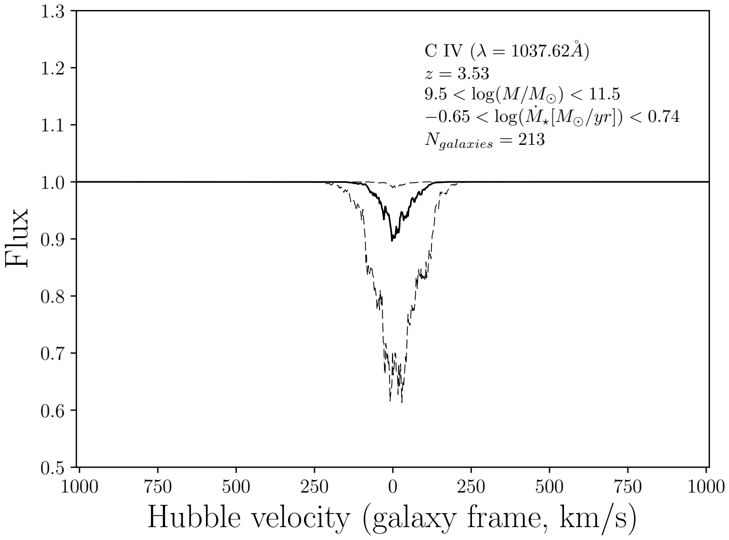

Figure 5.6: *The flux corresponding to Figure 5.5.*

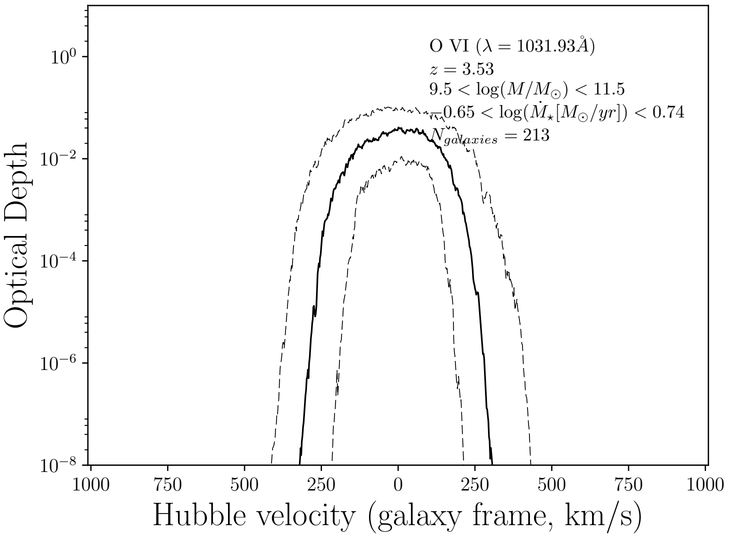

__Figure 5.7:__ The composite optical depths associated with O VI absorption from lines-of-sight passing through the CGM of the galaxies in the class whose definition is informed by a recent set of observations.

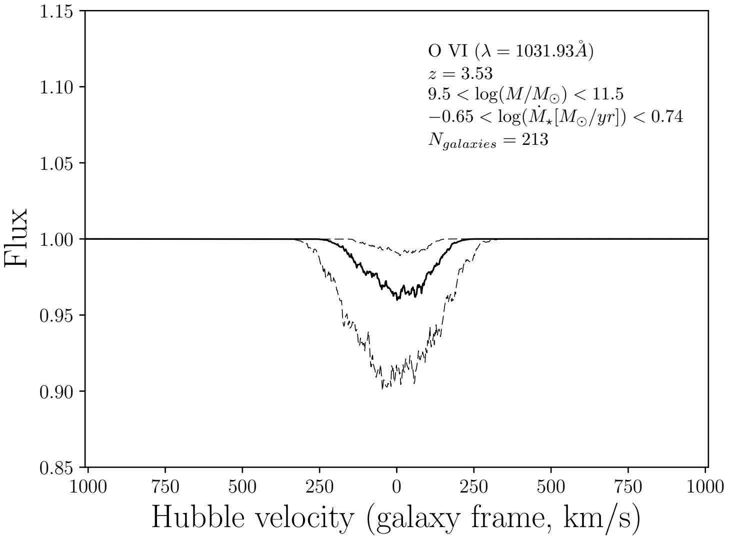

__Figure 5.8:__ The flux corresponding to Figure 5.7.

Version of July 29, 2019– Created July 29, 2019 - 00:59

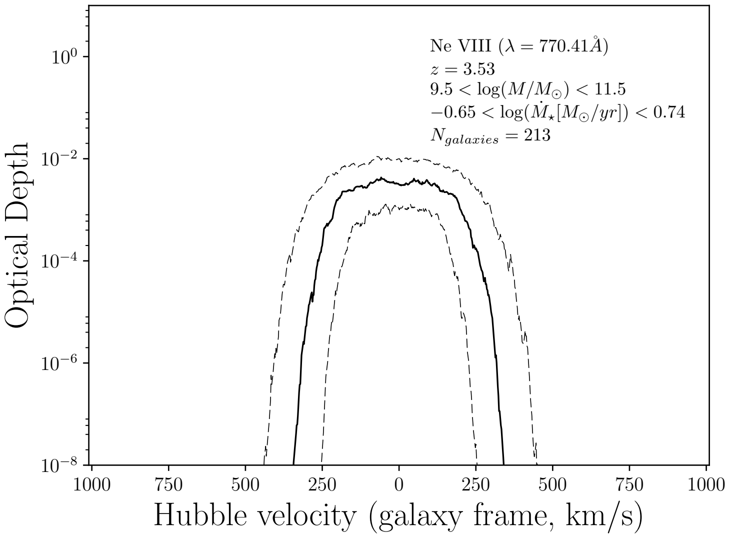

__Figure 5.9:__ The composite optical depths associated with Ne VIII absorption from lines-of-sight passing through the CGM of the galaxies in the class whose definition is informed by a recent set of observations.

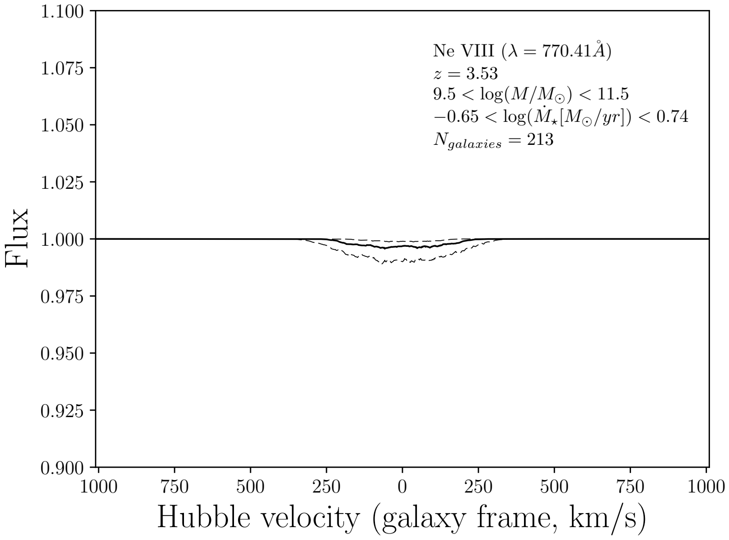

__Figure 5.10:__ The flux corresponding to Figure 5.9.

Chapter 6

Discussion

Generally speaking the aims of astrophysical simulations are two-fold: to confirm that artificially constructed cosmic ecosystems built upon prevailing physical theories align with what has been observed and to serve as a tool for probing phenomena in greater detail than what is attainable with observations. In this effort we have presented several results, but a discussion of what has not yet been answered and what could be worked out in the future is certainly warranted.

6.1 Unresolved Questions

The range of possible inquiries into the nature of the CGM of EAGLE galaxies is extensive. For the sake of brevity we explored an admittedly small region of parameter space while defining galaxy classes. While we present the radial profiles of central and satellite galaxies, star-forming and not star-forming, and binning measured values in physical and virial coordinates separately it would certainly be instructive to explore other galaxy classes to have a more comprehensive picture. Additionally, applying a statistical analysis regimen to the results from different galaxy classes could give us a quantitative, rather than qualitative, comparison.

Once the optical depth and flux profiles are extracted by the SpecWizard package for each pencil beam the peculiar velocities along the line-of-sight are computed. We use the value associated with the primary galaxy through which the line-of-sight passes to indicate the galaxy's location in velocity space. In Figure 4.2 we only incorporate the peculiar velocity value for the primary galaxy and the others are unchanged; a more systematic approach to dealing with the galaxies not being investigated that lie along the line-of-sight would be beneficial to future studies. Over large samples of pencil beams the contributions from nearby galaxies could perhaps be suppressed but it would be interesting to see to what extent the varying environments along the lines-of-sight affect these optical depth and flux profiles.

In Chapter 5 we present a single method of finding a line-of-sight passing through the CGM, namely with a random number generator which provides polar coordinates biased towards small impact parameters. Exploring additional methods, such as analyzing lines-of-sight at a fixed impact parameter (e.g., $0.5R_{\text{vir}}$) or with uniform sampling of the impact parameter we could determine to what extent this sampling process affects our composite optical depth and flux profiles. Additionally, it is common practice to use multiple lines-of-sight passing through the same galaxy during observations (Manuwal et al., 2019); this principle could be readily implemented into our code and provide even more lines-of-sight to analyze.

6.2 Future Work

Perhaps the most exciting aspect of working with the EAGLE data is that there is what appears to be a myriad of potential research questions waiting to be answered. From this thesis alone we could extend our analysis to additional classes (e.g., higher mass), other galactic material such as dark matter, and to higher redshifts; EAGLE has snapshots available up to redshift $z = 20$. With the usage of other simulations such as the high-resolution, 100 cMpc box we could in principle determine the dependencies of the presented analysis on number of galaxies in the class or SPH particle resolution. As alluded to in Chapter 2, a computational astrophysicist must always be aware of when it is advisable to sacrifice accuracy for a decrease in computational expense. The number of possible contingencies associated with this work necessitated an admittedly restrictive choice in galaxy class definitions and consequent analyses of available EAGLE simulations.

Machine learning algorithms could be applied to EAGLE in order to

Version of July 29, 2019– Created July 29, 2019 - 00:59

accelerate data analysis pipelines and provide more streamlined observation comparison processes. Let us say, for example, that observations have yielded a C IV column density radial profile for a single galaxy whose total mass and specific star formation rate are poorly understood. By feeding a deep, convolutional neural network with thousands of profiles from EAGLE galaxies similar to those found in Chapter 3 and the appendix we could develop an infrastructure that estimates to which class that galaxy belongs (Krizhevsky et al., 2012). With the `L0025N0752` box such a classifier would be most successful with central, low-mass galaxies at high redshift. To confirm that the galaxy does indeed belong to that class an absorption spectrum could be measured and compared to the results presented in Chapter 5.

The following ideas are entirely speculative but it is worth considering if utilizing a particular advancement in computing technology is a worthwhile venture for someone interested in astrophysical simulations at any scale. The Lattice Boltzmann Method, which was briefly introduced in Chapter 1, allows for the simulation of complex fluid flows by greatly reducing the number of degrees of freedom via two key ingredients: a mesoscopic treatment of the fluid particles and by constraining their flow through a lattice structure. If it is possible to create a formalism such that the lattice could be used as an octree-like framework for a gravity solver then the two primary forces governing astrophysical evolution could be implemented simultaneously in an environment ideally suited for graphical processing units, whose capabilities are improving dramatically given their association with deep learning.

Chapter 7

Conclusion

For most of human history our collective understanding of galactic astronomy was informed exclusively by the bright band across the night sky, the signature of the Milky Way. Ever since Hubble determined that this was only a very small part of the entire picture, astronomers have begun to fill in the tableau that is the structure of the cosmos. Filaments of intergalactic material and archipelagos of galaxies have coalesced from small density perturbations imprinted during the earliest moments in the Universe. These structures, teeming with complexity, can only be understood through rigorous observation programs and equally rigorous testing of the underlying physics using state-of-the-art computer simulations.

One of the more elusive elements of galaxies, their circumgalactic medium, is one of the most critical environments through which we can come to understand the processes of galaxy formation and evolution. The CGM is multiphase, has temperatures and densities which vary by orders of magnitude, and is driven to change rapidly in response to extreme phenomena like supernovae and supermassive black hole feedback. As a result, analysis of the CGM yields critical information about the galaxy as a whole in addition to critical tests of the physical theories underlying our understanding of how the cosmos operates.

In this thesis we explored the nature of the CGM surrounding low-mass, star-forming galaxies from within simulated regions millions of light-years across. Given the scale of the simulation suite we were able to analyze tens of thousands of synthetic galaxies in an effort to explain their composition, how they evolve, and how they relate to one another. This was achieved by breaking up the region into ”slices”, projecting the constituent material of each slice, and selecting out pixels belonging to the galaxies of interest. Pixels were binned by impact parameter such that composite radial profiles of quantities such as ion column density or metallicity could be produced for a class of galaxies. Generally speaking we found that our profiles qualitatively matched observations that have been presented in the literature.

Algorithms that distill the EAGLE data into formats similar to those presented in observation studies are critical; the SpecWizard package employed in Chapters 4 and 5 reads in the SPH particle data and produces line-of-sight measurements that are suitable for comparisons to observations. We present a proof of concept in Chapter 4 by analyzing a single line-of-sight as well as stacked lines-of-sight passing through the centers of galaxies belonging to a broadly-defined class at high redshift. Once the method of stacking has been established we provide the composite lines-of-sight optical depth and flux profiles passing through the circumgalactic media of galaxies belonging to a class for which observations will soon be available. Preliminary comparisons are encouraging, which buoys the idea that by delving further into the EAGLE data in ways that cannot be replicated with telescopes we could perhaps discover new things that have not yet been observed.

It is tremendously exciting to present a new analysis of the CGM at this point in the history of astronomical research. Given the number of proposed observational programs to be developed in the coming years we look forward to answering the call for continued research from a theoretical and computational perspective.

Chapter 8

Acknowledgements

This research was made possible by financial support from Leiden University. I would like to thank my advisors, Nastasha Wijers and Joop Schaye, for their tireless support during the course of this year-long project. If not for their advice and guidance this project would not have been possible. I would also like to thank Marius Cautun for acting as second corrector during the evaluation process of this thesis. To Mom and Dad, I could never thank you enough for your love and encouragement.

Chapter 9

Appendix

Codes written specifically written for this project are stored in the form of a GitHub repository: `https://github.com/BrianTCook/firstproject-CGM`. Within the main chapters of this thesis we have selected just a few figures from our entire analysis for the sake of brevity. In this appendix we present the radial profiles for the remaining galaxy classes. Chapter 3 provides these profiles strictly as a fraction of the virial radius; here we provide the analogous profiles when the appropriate values are binned by physical distance in §9.1. In Chapter 4 only the H I optical depths/fluxes are shown, but we computed similar quantities for the following metals: C IV, Si IV, O VI, and Ne VIII. These composite measurements are provided in §9.2. Lastly, the galaxy population table for the `L0025N0752` box is provided in §9.3.

9.1 H I/C IV/Si IV Column Densities and Covering Fractions

In §3.1, 3.2 we presented the column densities and associated covering fractions of H I, C IV, and Si IV in central, star-forming galaxies. These galaxies were separated into five total mass bins and these radial profiles are as a fraction of the virial radius. This section of the appendix is devoted to satellite galaxies, non-star-forming galaxies, in addition to presenting radial profiles where the relevant pixels were placed according to their physical distance. This method is more common in observations so these profiles may be more readily compared to observational studies.

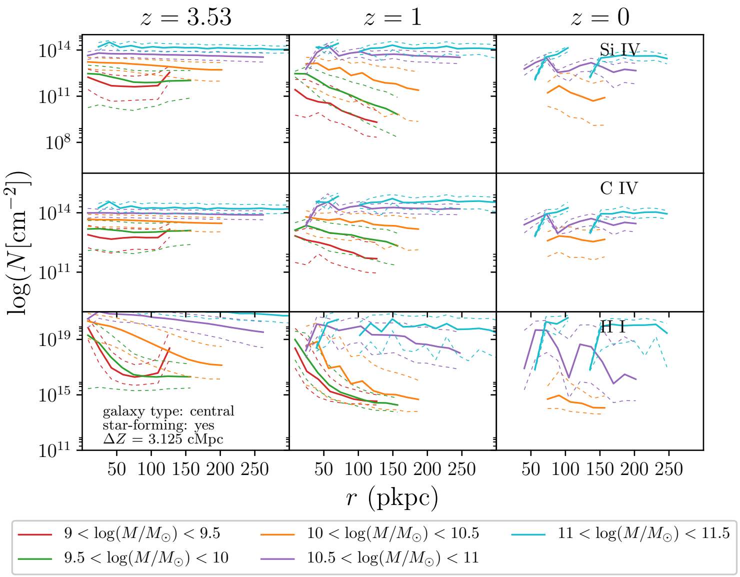

Figure 9.1: *The column densities of star-forming, central galaxies the relevant annuli are stored by physical distance rather than as a fraction of the virial radius.*

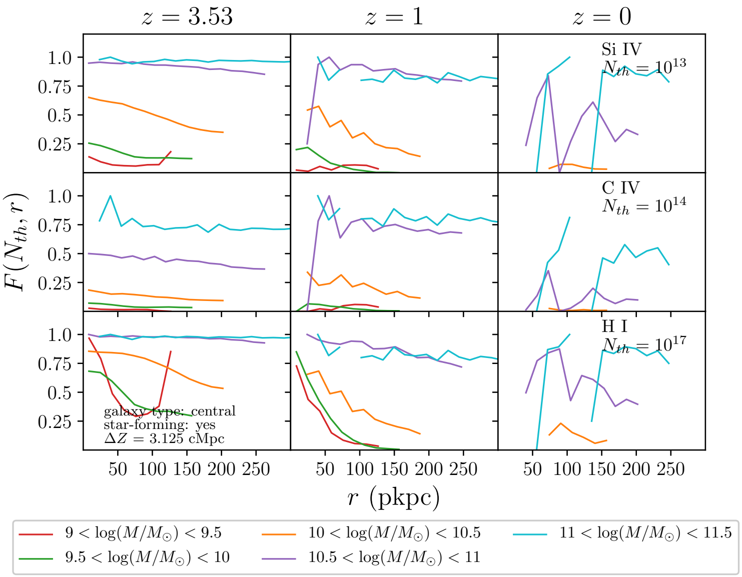

Figure 9.2: *The covering fractions for galaxies represented in Figure 9.1.*

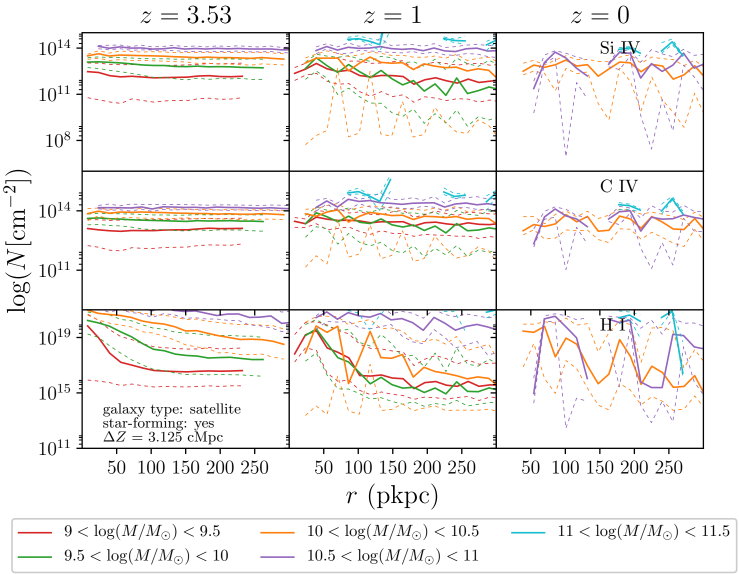

Figure 9.3: *The column densities of star-forming, satellite galaxies in physical coordinates.*

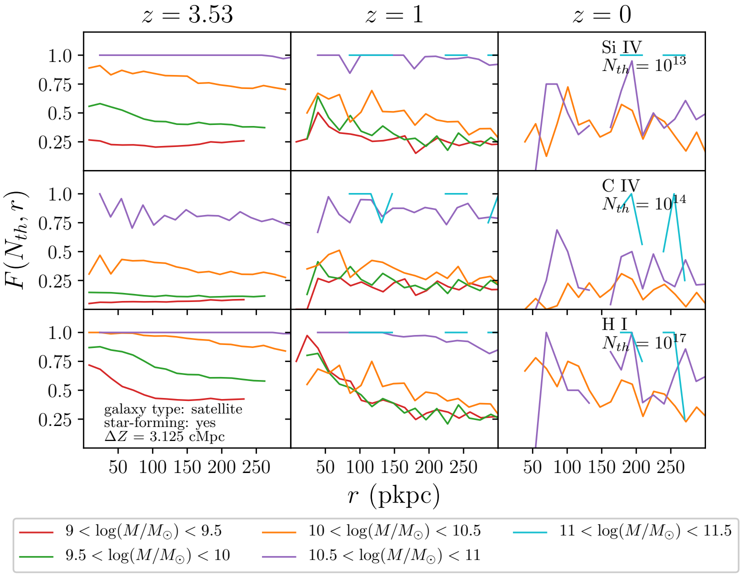

Figure 9.4: *The covering fractions for galaxies represented in Figure 9.3.*

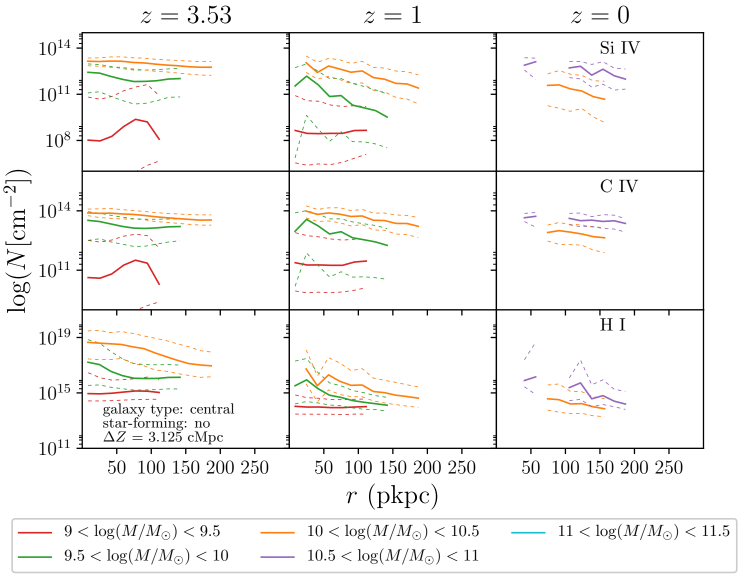

Figure 9.5: *The column densities of non star-forming ($\dot{M}_\odot < 10^{-11} M_\odot$/yr), central galaxies in physical coordinates.*

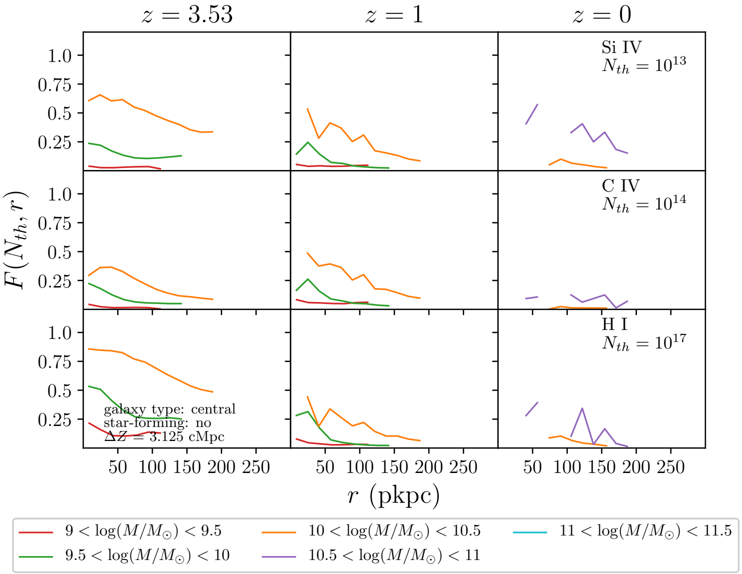

Figure 9.6: *The covering fractions for galaxies represented in Figure 9.3.*

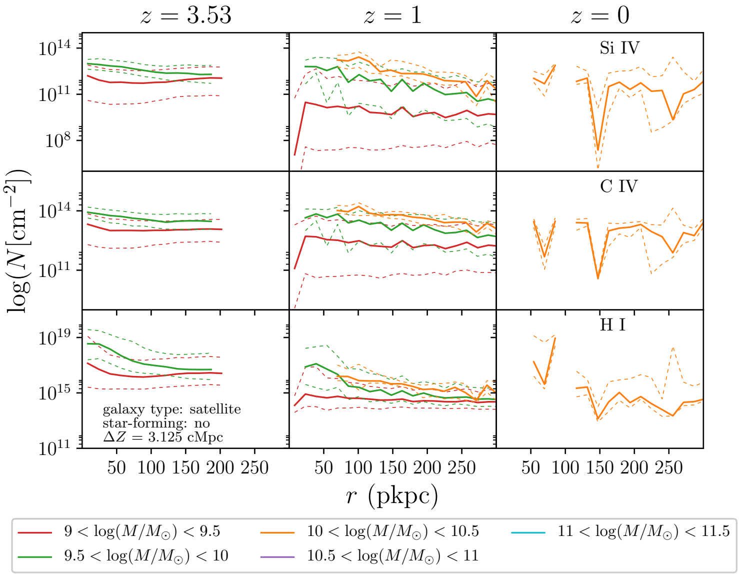

Figure 9.7: *The column densities of non star-forming ($\dot{M}_\odot < 10^{-11} M_\odot/\mathrm{yr}$), satellite galaxies in physical coordinates.*

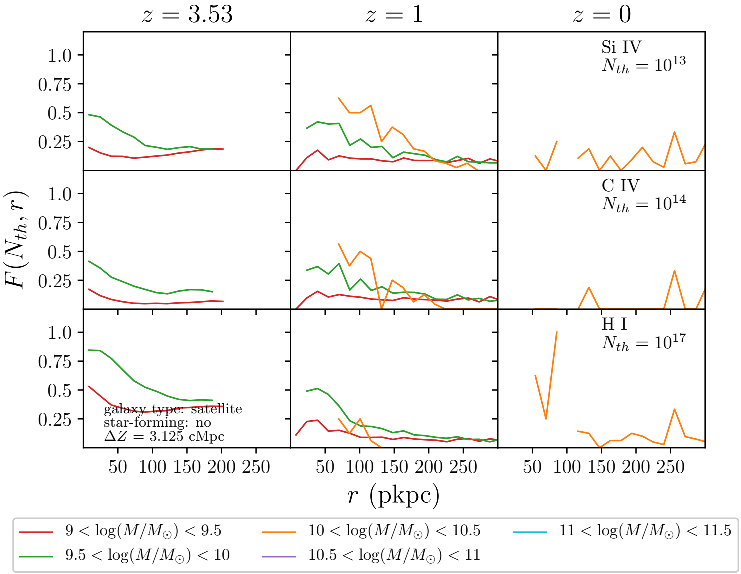

Figure 9.8: *The covering fractions for galaxies represented in Figure 9.7.*

9.1.1 Metallicity/Density/Temperature

Several Si IV-weighted local quantities are presented in §3.3 for central, star-forming galaxies. The plots in this section of the appendix show the radial profiles for other galaxy classes as well as the results for when the galaxies are analyzed by physical distance rather than as a fraction of the virial radius.

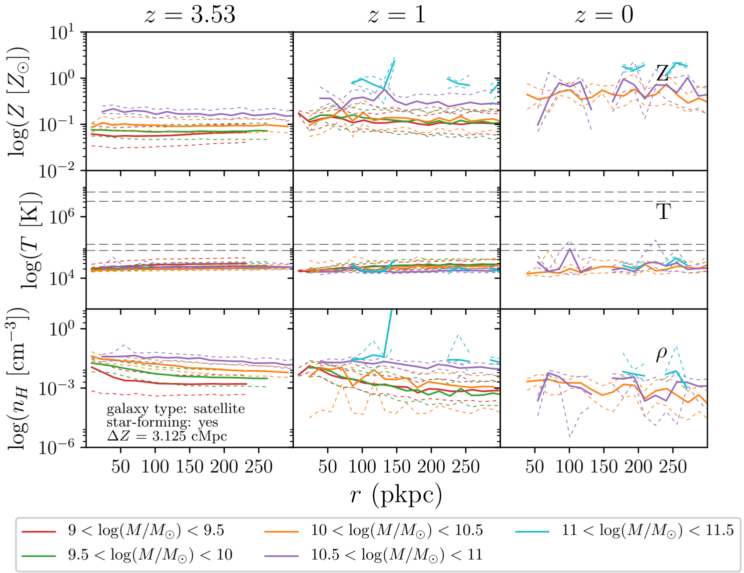

Figure 9.9: *The Si IV-weighted metallicity, temperature, and density of the star-forming, satellite galaxies where the impact parameter is in physical, rather than virial, coordinates.*

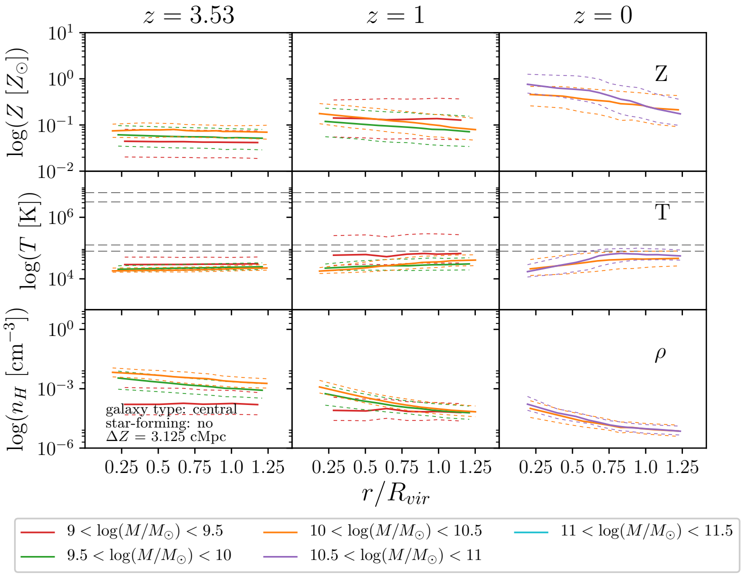

Figure 9.10: *The Si IV-weighted metallicity, temperature, and density of the non-star-forming, central galaxies where the impact parameter is as a fraction of* R_{vir}.

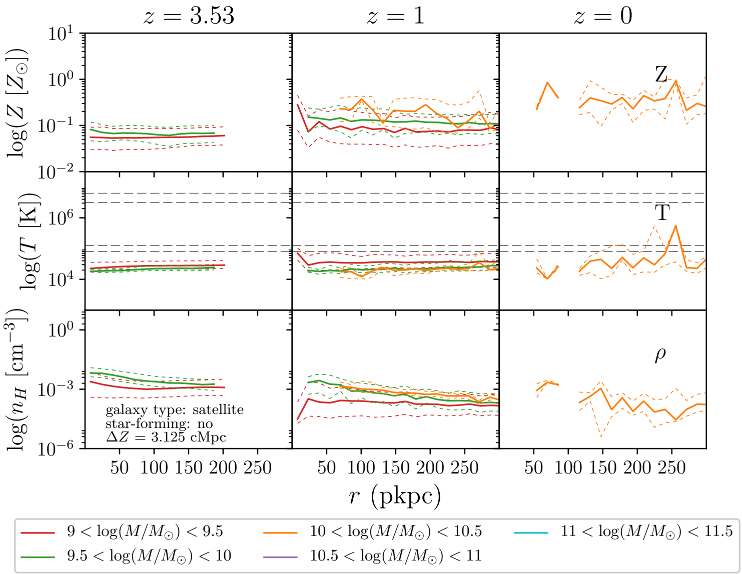

Figure 9.11: *The Si IV-weighted metallicity, temperature, and density radial profiles of the non-star-forming, satellite galaxies in pkpc.*

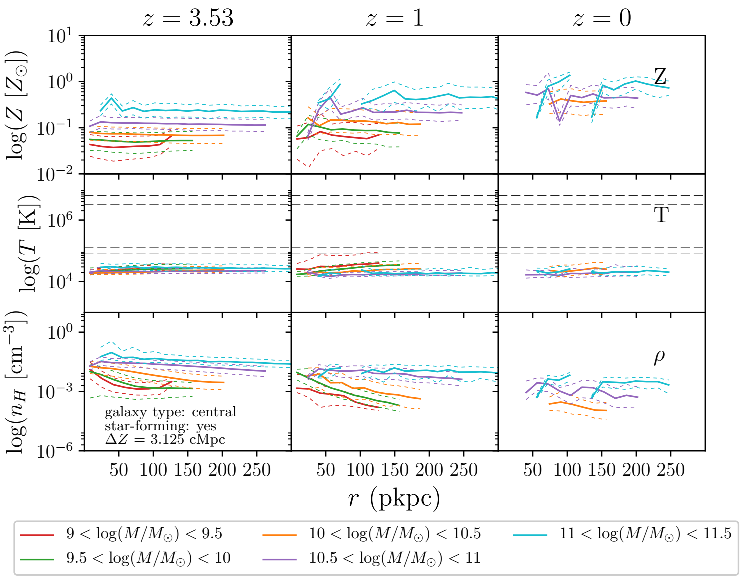

Figure 9.12: *The Si IV-weighted metallicity, temperature, and density radial profiles of the star-forming, central galaxies where the impact parameter is in pkpc.*

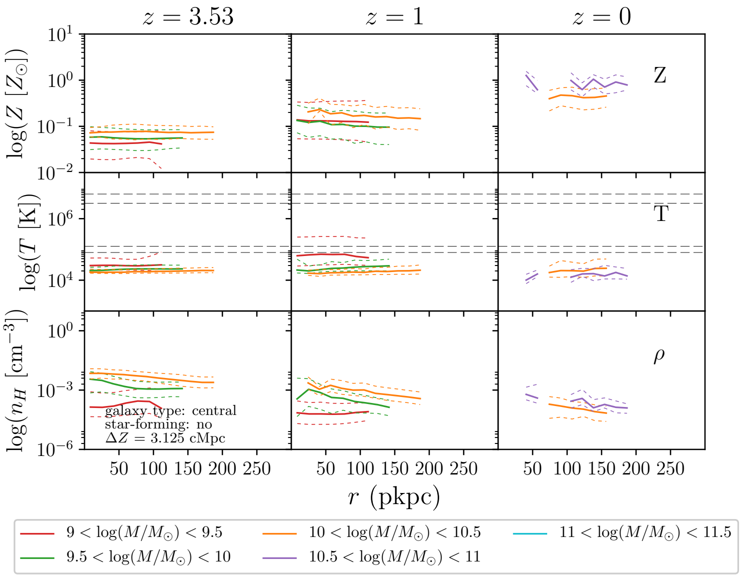

Figure 9.13: *The Si IV-weighted metallicity, temperature, and density of the non-star-forming, central galaxies where the impact parameter is in physical coordinates.*

Version of July 29, 2019– Created July 29, 2019 - 00:59

9.2 Metal Absorption Spectra

In chapter 4 the method of extracting pencil beam optical depth and flux profiles from the EAGLE data is discussed and as a proof-of-concept we show how a composite profile could be compiled using a ”stacking” method. Here we show the corresponding optical depth and flux profiles for O VI, Si IV, C IV, and Ne VIII.

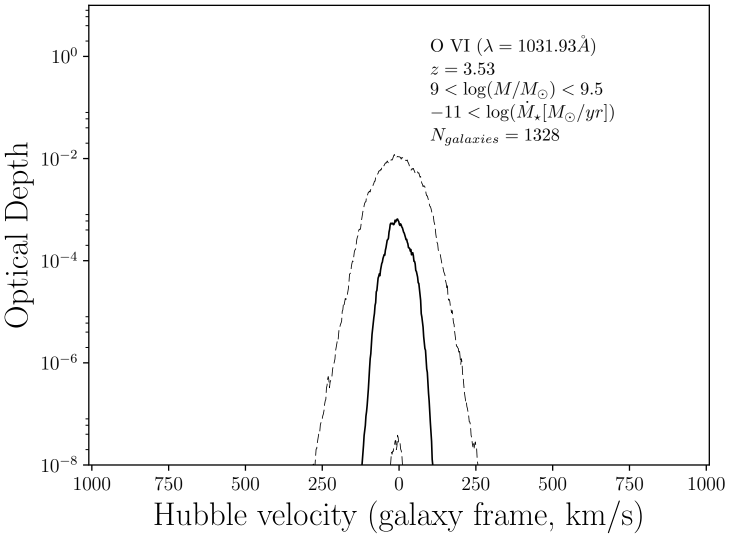

Figure 9.14: *The optical depth associated with photons that interact with O VI ions within the galaxies of Chapter 4.*

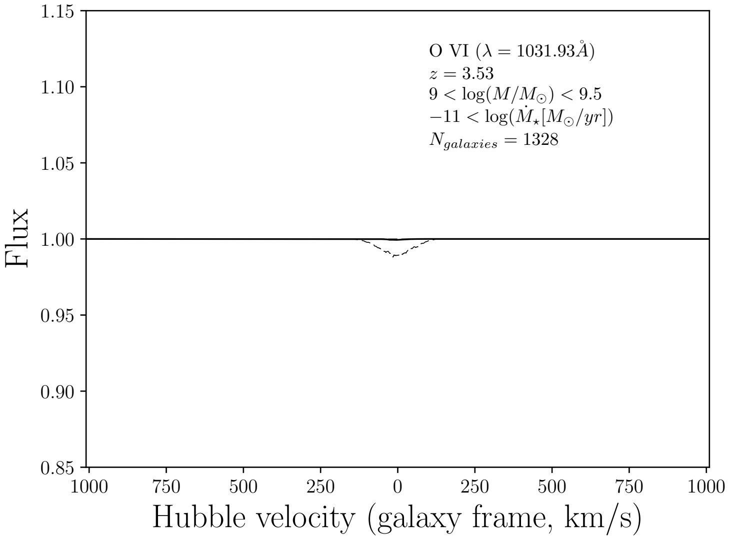

Figure 9.15: *The flux of photons absorbed by O VI along the line-of-sight passing through the center of each galaxy within the class discussed in Chapter 4.*

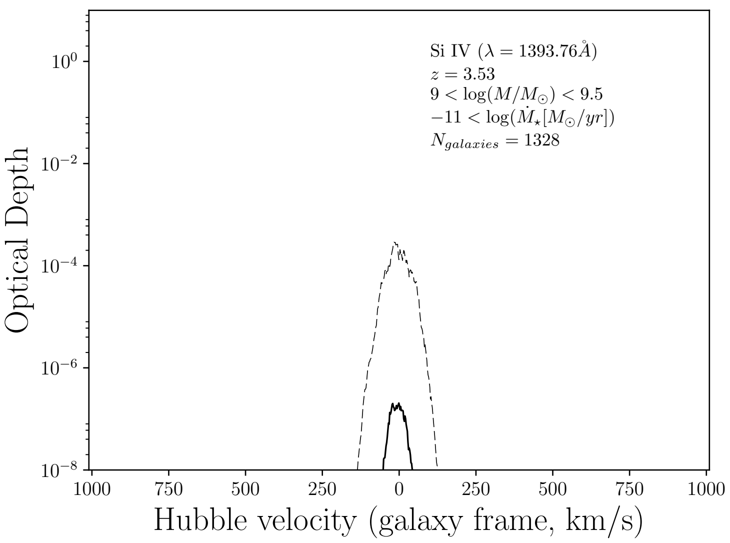

Figure 9.16: *The composite Si IV optical depth along the lines-of-sight passing through the galaxies of Chapter 4.*

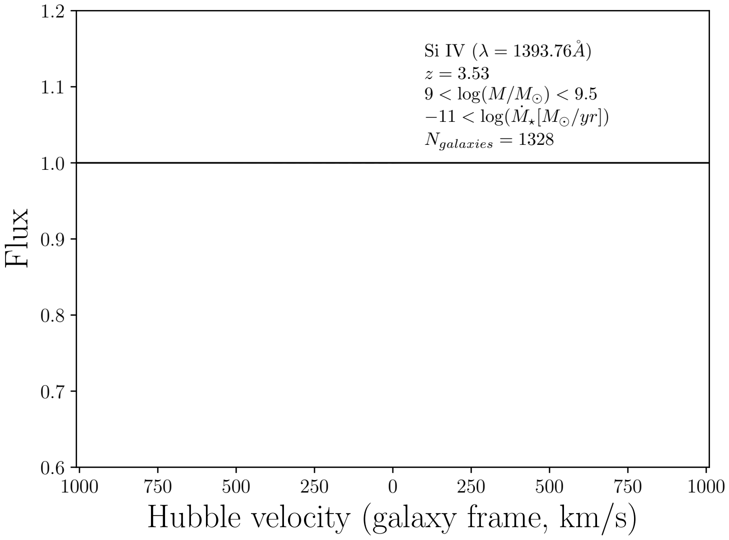

Figure 9.17: *The flux of photons absorbed by Si IV along the line-of-sight passing through the center of each galaxy within the class discussed in Chapter 4.*

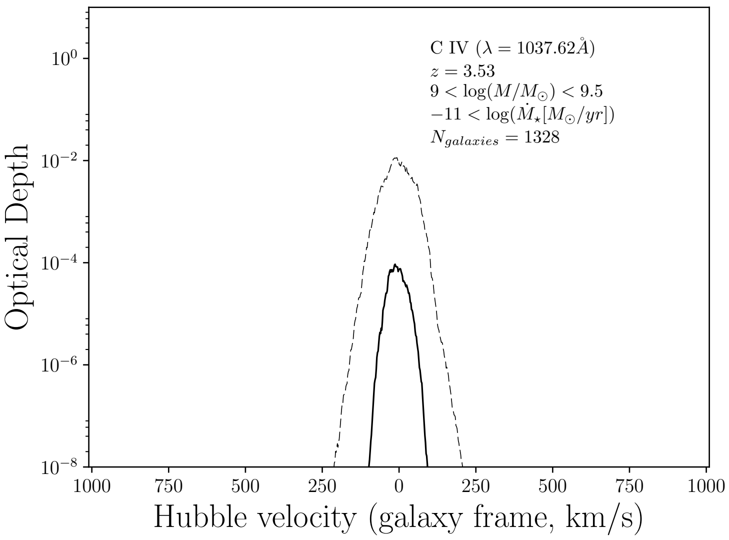

Figure 9.18: *The composite C IV optical depth along the lines-of-sight passing through the galaxies of Chapter 4.*

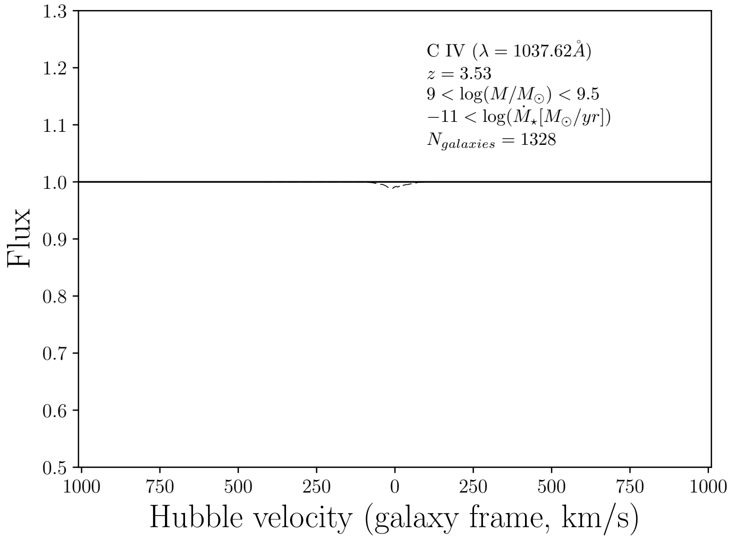

__Figure 9.19:__ The flux of photons absorbed by C IV along the line-of-sight passing through the center of each galaxy within the class discussed in Chapter 4.

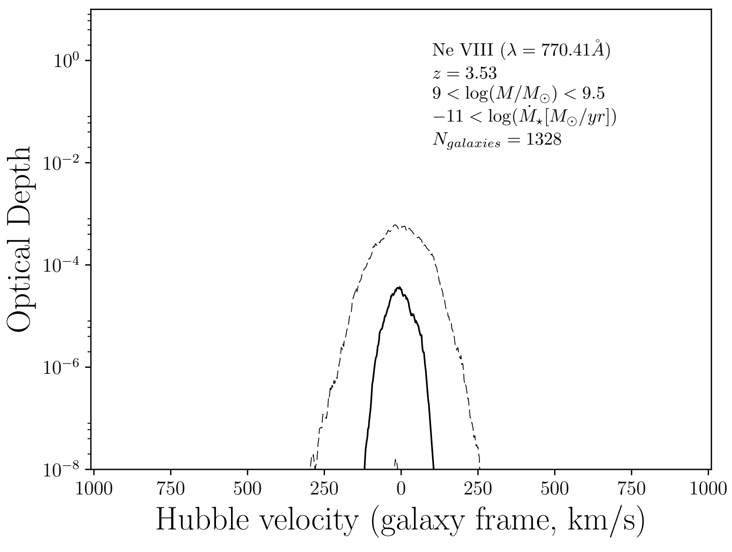

__Figure 9.20:__ The composite Ne VIII optical depth along the lines-of-sight passing through the galaxies of Chapter 4.

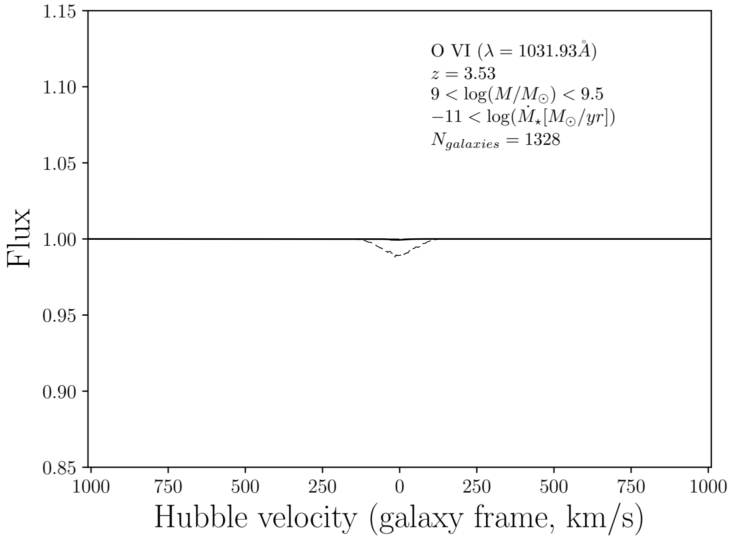

Figure 9.21: *The flux of photons absorbed by Ne VIII along the line-of-sight passing through the center of each galaxy within the class discussed in Chapter 4.*

9.3 Number of Galaxies in Each Class

All of the relevant galaxy population information for the `L0025N0752` box is shown in Table 9.1, which was the basis for the analyses presented in Chapter 2, Chapter 3, and §9.1. In some cases there were no galaxies available (e.g., very low-mass and star-forming central galaxies at $z = 0$). Some of the more erratic plots presented in §9.1 may be attributed to poor galaxy sampling; for example, there are three galaxy types where three or fewer galaxies were analyzed. Future research could be devoted to these poorly sampled galaxy classes by using a larger EAGLE simulation like the `L100N1504` box. The sixth column indicates how many galaxies are present in the box while the fifth column shows how many were kept after the slicing method was implemented.

z	$\left(x < \log\left(\frac{M}{M_\odot}\right) < y\right)$	Star Forming	Type	$N^\star_{\text{galaxies}}$	$N_{\text{galaxies,total}}$
3.53	9.5, 10	yes	central	1501	1559
3.53	10, 10.5	yes	central	732	775
3.53	10.5, 11	yes	central	212	224
3.53	11, 11.5	yes	central	65	72
1	9, 9.5	yes	central	11	11
1	9.5, 10	yes	central	93	94
1	10, 10.5	yes	central	471	488
1	10.5, 11	yes	central	320	349
1	11, 11.5	yes	central	117	129
0	10, 10.5	yes	central	245	252
0	10.5, 11	yes	central	303	320
0	11, 11.5	yes	central	116	126
3.53	9, 9.5	yes	central	1292	1328
3.53	9, 9.5	yes	satellite	436	472
3.53	9.5, 10	yes	satellite	213	233
3.53	10, 10.5	yes	satellite	47	52
3.53	10.5, 11	yes	satellite	10	12
3.53	11, 11.5	yes	satellite	1	1
1	9, 9.5	yes	satellite	133	140
1	9.5, 10	yes	satellite	167	184
1	10, 10.5	yes	satellite	84	101
1	10.5, 11	yes	satellite	38	43
1	11, 11.5	yes	satellite	10	15
0	10, 10.5	yes	satellite	86	92
0	10.5, 11	yes	satellite	67	75
0	11, 11.5	yes	satellite	19	23
3.53	9, 9.5	no	central	6999	7171
3.53	9.5, 10	no	central	962	986
3.53	10, 10.5	no	central	28	30
1	9, 9.5	no	central	515	525
1	9.5, 10	no	central	170	176
1	10, 10.5	no	central	165	173
0	10, 10.5	no	central	210	215
0	10.5, 11	no	central	15	18
3.53	9, 9.5	no	satellite	532	554
3.53	9.5, 10	no	satellite	30	35
1	9, 9.5	no	satellite	486	581
1	9.5, 10	no	satellite	89	102
1	10, 10.5	no	satellite	2	4
0	10, 10.5	no	satellite	31	34
0	10.5, 11	no	satellite	3	3

Table 9.1: *The number of galaxies in the `L0025N0752` box with the indicated attributes. The sixth column corresponds to the total number while the fifth column accounts for the galaxies that have to be omitted as they are too close to a slice boundary. The slice boundaries in the* $\Delta Z = 3.125$ *case are at* $Z = 3.125 \times n$*, where* $n \in [0, 8]$.

Bibliography

Baek, S., B. Semelin, P. Di Matteo, Y. Revaz, and F. Combes (2010, Nov). Reionization by UV or X-ray sources. *523*, A4.

Baes, M., A. Trčka, P. Camps, A. Nersesian, J. Trayford, T. Theuns, and W. Dobbels (2019, January). The cosmic spectral energy distribution in the EAGLE simulation. *Monthly Notices of the Royal Astronomical Society 484*(3), 4069–4082.

Barnes, J. and P. Hut (1986, December). A hierarchical O(N log N) force-calculation algorithm. *324*, 446–449.

Benítez-Llambay, P. and F. S. Masset (2016, March). FARGO3d: A NEW GPU-ORIENTED MHD CODE. *The Astrophysical Journal Supplement Series 223*(1), 11.

Berlok, T. and C. Pfrommer (2019, February). On the kelvin–helmholtz instability with smooth initial conditions – linear theory and simulations. *Monthly Notices of the Royal Astronomical Society 485*(1), 908–923.

Bielby, R. M., J. P. Stott, F. Cullen, T. M. Tripp, J. N. Burchett, M. Fumagalli, S. L. Morris, N. Tejos, R. A. Crain, and R. G. Bower (2019, Jun). Quasar Sightline and Galaxy Evolution (QSAGE) survey - I. The galaxy environment of O VI absorbers up to z = 1.4 around PKS 0232-04. *486*(1), 21–41.

Bryan, G. L., M. L. Norman, B. W. OShea, T. Abel, J. H. Wise, M. J. Turk, D. R. Reynolds, D. C. Collins, P. Wang, S. W. Skillman, B. Smith, R. P. Harkness, J. Bordner, J. hoon Kim, M. Kuhlen, H. Xu, N. Goldbaum,

C. Hummels, A. G. Kritsuk, E. Tasker, S. Skory, C. M. Simpson, O. Hahn, J. S. Oishi, G. C. So, F. Zhao, R. Cen, and Y. L. and (2014, March). ENZO: AN ADAPTIVE MESH REFINEMENT CODE FOR ASTROPHYSICS. *The Astrophysical Journal Supplement Series 211*(2), 19.

Cen, R.-y., J. Miralda-Escude, J. P. Ostriker, and M. Rauch (1994). Gravitational collapse of small scale structure as the origin of the Lyman alpha forest. *Astrophys. J. 437*, L9.

Chen, H.-W. (2012, Dec). The unchanging circumgalactic medium over the past 11 billion years. *427*(2), 1238–1244.

Cochrane, R. K., P. N. Best, D. Sobral, I. Smail, J. E. Geach, J. P. Stott, and D. A. Wake (2018, January). The dependence of galaxy clustering on stellar mass, star-formation rate and redshift at z = 0.8–2.2, with HiZELS. *Monthly Notices of the Royal Astronomical Society 475*(3), 3730–3745.

Conselice, C. J. (2014, August). The evolution of galaxy structure over cosmic time. *Annual Review of Astronomy and Astrophysics 52*(1), 291–337.

Crain, R. A., J. Schaye, R. G. Bower, M. Furlong, M. Schaller, T. Theuns, C. D. Vecchia, C. S. Frenk, I. G. McCarthy, J. C. Helly, A. Jenkins, Y. M. Rosas-Guevara, S. D. M. White, and J. W. Trayford (2015, April). The EAGLE simulations of galaxy formation: calibration of subgrid physics and model variations. *Monthly Notices of the Royal Astronomical Society 450*(2), 1937–1961.

Dawoodbhoy, T., P. R. Shapiro, P. Ocvirk, D. Aubert, N. Gillet, J.-H. Choi, I. T. Iliev, R. Teyssier, G. Yepes, S. Gottlöber, A. D'Aloisio, H. Park, and Y. Hoffman (2018, July). Suppression of star formation in low-mass galaxies caused by the reionization of their local neighbourhood. *Monthly Notices of the Royal Astronomical Society 480*(2), 1740–1753.

de Graaff, A., Y.-C. Cai, C. Heymans, and J. A. Peacock (2019, Apr). Probing the missing baryons with the Sunyaev-Zel'dovich effect from filaments. *624*, A48.

Dolag, K. and F. Stasyszyn (2009, October). An MHD gadget for cosmological simulations. *Monthly Notices of the Royal Astronomical Society 398*(4), 1678–1697.

Emerick, A., G. L. Bryan, M.-M. Mac Low, B. Côté, K. V. Johnston, and B. W. O'Shea (2018, Dec). Metal Mixing and Ejection in Dwarf Galaxies Are Dependent on Nucleosynthetic Source. *869*(2), 94.

Fukushige, T., J. Makino, and A. Kawai (2005, Dec). GRAPE-6A: A Single-Card GRAPE-6 for Parallel PC-GRAPE Cluster Systems. *57*, 1009–1021.

Gunn, J. E. and B. A. Peterson (1965, November). On the Density of Neutral Hydrogen in Intergalactic Space. *142*, 1633–1636.

Heckman, T. M., M. D. Lehnert, D. K. Strickland , and L. Armus (2000, Aug). Absorption-Line Probes of Gas and Dust in Galactic Superwinds. *129*(2), 493–516.

Hubble, E. P. (1925). Cepheids in Spiral Nebulae. *Popular Astronomy 33*.

Ilbert, O., H. J. McCracken, O. Le Fèvre, P. Capak, J. Dunlop, A. Karim, M. A. Renzini, K. Caputi, S. Boissier, S. Arnouts, H. Aussel, J. Comparat, Q. Guo, P. Hudelot, J. Kartaltepe, J. P. Kneib, J. K. Krogager, E. Le Floc'h, S. Lilly, Y. Mellier, B. Milvang-Jensen, T. Moutard, M. Onodera, J. Richard, M. Salvato, D. B. Sanders, N. Scoville, J. D. Silverman, Y. Taniguchi, L. Tasca, R. Thomas, S. Toft, L. Tresse, D. Vergani, M. Wolk, and A. Zirm (2013, August). Mass assembly in quiescent and star-forming galaxies since z 4 from UltraVISTA. *556*, A55.

Kaiser, N. (1987, July). Clustering in real space and in redshift space. *227*, 1–21.

Kitchin, C. R. (1987). *Stars, nebulae and the interstellar medium. Observational physics and astrophysics*.

Krizhevsky, A., I. Sutskever, and G. E. Hinton (2012). Imagenet classification with deep convolutional neural networks. In F. Pereira, C. J. C. Burges, L. Bottou, and K. Q. Weinberger (Eds.), *Advances in Neural Information Processing Systems 25*, pp. 1097–1105. Curran Associates, Inc.

Lau, M. W., J. X. Prochaska, and J. F. Hennawi (2018, April). Quasars probing quasars. IX. the kinematics of the circumgalactic medium surrounding z $\sim$ 2 quasars. *The Astrophysical Journal 857*(2), 126.

Lebouteiller, V., D. Kunth, J. Roman-Duval, P. Richter, C. Gry, B. James, and A. Aloisi (2019, May). ISM and CGM in external galaxies. In , Volume 51, pp. 157.

Lehner, N., J. N. Burchett, J. C. Howk, J. M. O'Meara, M. S. Peeples, M. Rafelski, J. Ribaudo, and S. Tuttle (2019, May). Following the Metals in the Intergalactic and Circumgalactic Medium over Cosmic Time. In , Volume 51, pp. 473.

Leitner, S. N. (2012, January). ON THE LAST 10 BILLION YEARS OF STELLAR MASS GROWTH IN STAR-FORMING GALAXIES. *The Astrophysical Journal 745*(2), 149.

Leonard, A., S. Pires, and J.-L. Starck (2012, May). Fast calculation of the weak lensing aperture mass statistic. *Monthly Notices of the Royal Astronomical Society 423*(4), 3405–3412.

LeVeque, R. J. (2011). *Finite volume methods for hyperbolic problems*. Cambridge Univ. Press.

Lockman, F. J., K. Jahoda, and D. McCammon (1986, March). The structure of galactic HI in directions of low total column density. *302*, 432–449.

Lynds, R. (1971, March). The Absorption-Line Spectrum of 4c 05.34. *164*, L73.

Manuwal, A., A. Narayanan, S. Muzahid, J. C. Charlton, V. Khaire, and H. Chand (2019, May). C IV absorbers tracing cool gas in dense galaxy group/cluster environments. *485*(1), 30–46.

Martis, N. S., D. Marchesini, G. B. Brammer, A. Muzzin, I. Labbé, I. G. Momcheva, R. E. Skelton, M. Stefanon, P. G. van Dokkum, and K. E. Whitaker (2016, Aug). The Evolution of the Fractions of Quiescent and Star-forming Galaxies as a Function of Stellar Mass Since z = 3: Increasing Importance of Massive, Dusty Star-forming Galaxies in the Early Universe. *827*(2), L25.

Moster, B. P., T. Naab, and S. D. M. White (2018, March). emerge – an empirical model for the formation of galaxies since z $\sim$ 10. *Monthly Notices of the Royal Astronomical Society 477*(2), 1822–1852.

Münch, G. and H. Zirin (1961, January). Interstellar Matter at Large Distances from the Galactic Plane. *133*, 11.

Muzahid, S. (2014, February). PROBING THE LARGE AND MASSIVE CIRCUMGALACTIC MEDIUM OF a GALAXY ATz∼ 0.2 USING a PAIR OF QUASARS. *The Astrophysical Journal 784*(1), 5.

Muzahid, S., R. Srianand, J. Charlton, and M. Eracleous (2016, February). On the covering fraction variability in an EUV mini-BAL outflow from PG 1206459. *Monthly Notices of the Royal Astronomical Society 457*(3), 2665–2674.

Nicastro, F., J. Kaastra, Y. Krongold, S. Borgani, E. Branchini, R. Cen, M. Dadina, C. W. Danforth, M. Elvis, F. Fiore, A. Gupta, S. Mathur, D. Mayya, F. Paerels, L. Piro, D. Rosa-Gonzalez, J. Schaye, J. M. Shull, J. Torres-Zafra, N. Wijers, and L. Zappacosta (2018, June). Observations of the missing baryons in the warm–hot intergalactic medium. *Nature 558*(7710), 406–409.

Nielsen, N. M., G. G. Kacprzak, S. Muzahid, C. W. Churchill, M. T. Murphy, and J. C. Charlton (2017, Jan). The Highly Ionized Circumgalactic Medium is Kinematically Uniform around Galaxies. *834*(2), 148.

Oppenheimer, B., J. Kollmeier, A. Kravtsov, J. Bregman, D. Angles-Alcazar, R. Crain, R. Dave, L. Hernquist, C. Hummels, and J. Schaye (2019, May). Imprint of Drivers of Galaxy Formation in the Circumgalactic Medium. In , Volume 51, pp. 280.

Oppenheimer, B. D., R. A. Crain, J. Schaye, A. Rahmati, A. J. Richings, J. W. Trayford, J. Tumlinson, R. G. Bower, M. Schaller, and T. Theuns (2016, May). Bimodality of low-redshift circumgalactic o vi in non-equilibrium eagle zoom simulations. *Monthly Notices of the Royal Astronomical Society 460*(2), 2157–2179.

Oppenheimer, B. D., J. Schaye, R. A. Crain, J. K. Werk, and A. J. Richings (2018, August). The multiphase circumgalactic medium traced by low metal ions in EAGLE zoom simulations. *Monthly Notices of the Royal Astronomical Society 481*(1), 835–859.

Version of July 29, 2019– Created July 29, 2019 - 00:59

Pallottini, A., S. Gallerani, and A. Ferrara (2014, August). The circumgalactic medium of high-redshift galaxies. *Monthly Notices of the Royal Astronomical Society: Letters 444*(1), L105–L109.

Pisano, D. J., A. Fox, D. French, J. C. Howk, N. Lehner, F. J. Lockman, and K. Jones (2019, May). Completing the Hydrogen Census in the Circumgalactic Medium at z 0. In , Volume 51, pp. 568.

Premnath, K. N., M. J. Pattison, and S. Banerjee (2009, July). Dynamic subgrid scale modeling of turbulent flows using lattice-boltzmann method. *Physica A: Statistical Mechanics and its Applications 388*(13), 2640–2658.

Rahmati, A., A. H. Pawlik, M. Raičević, and J. Schaye (2013, April). On the evolution of the H I column density distribution in cosmological simulations. *430*, 2427–2445.

Robinson, J. (1996). *Atomic Spectroscopy, Second Edition,*. Taylor & Francis.

Rosswog, S. (2009, April). Astrophysical smooth particle hydrodynamics. *New Astronomy Reviews 53*(4-6), 78–104.

Rubin, K. H. R. (2017, Jan). Gas Accretion Traced in Absorption in Galaxy Spectroscopy. In A. Fox and R. Davé (Eds.), *Gas Accretion onto Galaxies*, Volume 430 of *Astrophysics and Space Science Library*, pp. 95.

Rudie, G. C., C. C. Steidel, M. Pettini, R. F. Trainor, A. L. Strom, C. B. Hummels, N. A. Reddy, and A. E. Shapley (2019, February). The Column Density, Kinematics, and Thermal State of Metal-Bearing Gas within the Virial Radius of z˜2 Star-Forming Galaxies in the Keck Baryonic Structure Survey. *arXiv e-prints*.

Sakurai, J. J., S. F. Tuan, and E. D. Commins (1995, Jan). Modern Quantum Mechanics, Revised Edition. *American Journal of Physics 63*(1), 93–95.

Schaller, M., C. D. Vecchia, J. Schaye, R. G. Bower, T. Theuns, R. A. Crain, M. Furlong, and I. G. McCarthy (2015, October). The eagle simulations of galaxy formation: the importance of the hydrodynamics scheme. *Monthly Notices of the Royal Astronomical Society 454*(3), 2277–2291.

Schaye, J., A. Aguirre, T.-S. Kim, T. Theuns, M. Rauch, and W. L. W. Sargent (2003, October). Metallicity of the intergalactic medium using pixel statistics. II. the distribution of metals as traced by civ. *The Astrophysical Journal 596*(2), 768–796.

Schaye, J., R. A. Crain, R. G. Bower, M. Furlong, M. Schaller, T. Theuns, C. D. Vecchia, C. S. Frenk, I. G. McCarthy, J. C. Helly, A. Jenkins, Y. M. Rosas-Guevara, S. D. M. White, M. Baes, C. M. Booth, P. Camps, J. F. Navarro, Y. Qu, A. Rahmati, T. Sawala, P. A. Thomas, and J. Trayford (2014, November). The EAGLE project: simulating the evolution and assembly of galaxies and their environments. *Monthly Notices of the Royal Astronomical Society 446*(1), 521–554.

Schmidt, M. (1963, March). 3C 273 : A Star-Like Object with Large Red-Shift. *197*, 1040.

Shen, S., P. Madau, J. Guedes, L. Mayer, J. X. Prochaska, and J. Wadsley (2013, February). THE CIRCUMGALACTIC MEDIUM OF MASSIVE GALAXIES ATz$\sim$ 3: A TEST FOR STELLAR FEEDBACK, GALACTIC OUTFLOWS, AND COLD STREAMS. *The Astrophysical Journal 765*(2), 89.

Somerville, R. S. and R. Davé (2015, August). Physical models of galaxy formation in a cosmological framework. *Annual Review of Astronomy and Astrophysics 53*(1), 51–113.

Sparre, M., C. Pfrommer, and M. Vogelsberger (2018, November). The physics of multiphase gas flows: fragmentation of a radiatively cooling gas cloud in a hot wind. *Monthly Notices of the Royal Astronomical Society 482*(4), 5401–5421.

Spitzer, Jr., L. (1956, July). On a Possible Interstellar Galactic Corona. *124*, 20.

Springel, V. (2005, December). The cosmological simulation code GADGET-2. *364*, 1105–1134.

Steidel, C. C., D. K. Erb, A. E. Shapley, M. Pettini, N. Reddy, M. Bogosavljević, G. C. Rudie, and O. Rakic (2010, Jul). The Structure and Kinematics of the Circumgalactic Medium from Far-ultraviolet Spectra of z ~= 2-3 Galaxies. *717*(1), 289–322.

Stinson, G. S., C. Brook, J. X. Prochaska, J. Hennawi, S. Shen, J. Wadsley, A. Pontzen, H. M. P. Couchman, T. Quinn, A. V. Macciò, and B. K. Gibson (2012, September). MAGICC haloes: confronting simulations with observations of the circumgalactic medium at z=0. *425*, 1270–1277.

Stone, J. (2007). Computational astrophysics. *Scholarpedia 2*(10), 2419.

Stone, J. M., T. A. Gardiner, P. Teuben, J. F. Hawley, and J. B. Simon (2008, September). Athena: A new code for astrophysical MHD. *The Astrophysical Journal Supplement Series 178*(1), 137–177.

The EAGLE team (2017, Jun). The EAGLE simulations of galaxy formation: Public release of particle data. *arXiv e-prints*, arXiv:1706.09899.

Theuns, T., A. Leonard, G. Efstathiou, F. R. Pearce, and P. A. Thomas (1998, December). P^3M-SPH simulations of the Lyalpha forest. *301*, 478–502.

Trimble, V. (1995, December). The 1920 Shapley-Curtis Discussion: Background, Issues, and Aftermath. *107*, 1133.

Tumlinson, J., M. S. Peeples, and J. K. Werk (2017, August). The circumgalactic medium. *Annual Review of Astronomy and Astrophysics 55*(1), 389–432.

Turner, E. L. and J. R. Gott, III (1976, November). Groups of galaxies. I. A catalog. *32*, 409–427.

Turner, M. L., J. Schaye, R. A. Crain, G. Rudie, C. C. Steidel, A. Strom, and T. Theuns (2017, June). A comparison of observed and simulated absorption from h i, c iv, and si iv around $z \approx 2$ star-forming galaxies suggests redshift–space distortions are due to inflows. *Monthly Notices of the Royal Astronomical Society 471*(1), 690–705.

van Son, L. A. C., C. Barber, Y. M. Bahé, J. Schaye, D. J. Barnes, R. A. Crain, S. T. Kay, T. Theuns, and C. D. Vecchia (2019, February). Galaxies with monstrous black holes in galaxy cluster environments. *Monthly Notices of the Royal Astronomical Society 485*(1), 396–407.

Wang, Q. D., J. N. Burchett, N. Lehner, J. M. O'Meara, M. S. Peeples, J. E. G. Peek, M. Rafelski, J. Tumlinson, J. Werk, and D. Zaritsky (2019, May). The Panchromatic Circumgalactic Medium. In , Volume 51, pp. 415.

Werk, J. K., J. X. Prochaska, S. Cantalupo, A. J. Fox, B. Oppenheimer, J. Tumlinson, T. M. Tripp, N. Lehner, and M. McQuinn (2016, December). THE COS-HALOS SURVEY: ORIGINS OF THE HIGHLY IONIZED CIRCUMGALACTIC MEDIUM OF STAR-FORMING GALAXIES. *The Astrophysical Journal 833*(1), 54.

Wijers, N. A., J. Schaye, B. D. Oppenheimer, R. A. Crain, and F. Nicastro (2019, Apr). The abundance and physical properties of O VII and O VIII X-ray absorption systems in the EAGLE simulations. *arXiv e-prints*, arXiv:1904.01057.

Zel'dovich, Y. B. (1970, March). Gravitational instability: An approximate theory for large density perturbations. *5*, 84–89.

Zheng, Y., M. E. Putman, J. E. G. Peek, and M. R. Joung (2015, July). The Circumgalactic Medium of the Milky Way is Half Hidden. *807*, 103.